

Classically Perfect Gauge Actions on Anisotropic Lattices ¹

Philipp Rüfenacht

Institute for Theoretical Physics, University of Bern
Sidlerstrasse 5, CH-3012 Bern, Switzerland

Urs Wenger

Theoretical Physics, Oxford University
1 Keble Road, Oxford OX1 3NP, United Kingdom

Abstract

We present a method for constructing classically perfect anisotropic actions for SU(3) gauge theory based on an isotropic Fixed Point Action. The action is parametrised using smeared (“fat”) links. The construction is done explicitly for anisotropy $\xi = a_s/a_t = 2$ and 4. The corresponding renormalised anisotropies are determined using the torelon dispersion relation. The renormalisation of the anisotropy is small and the parametrisation describes the true action well. Quantities such as the static quark-antiquark potential, the critical temperature of the deconfining phase transition and the low-lying glueball spectrum are measured on lattices with anisotropy $\xi = 2$. The mass of the scalar 0^{++} glueball is determined to be 1580(60) MeV, while the tensor 2^{++} glueball is at 2430(60) MeV.

¹Work supported in part by Schweizerischer Nationalfonds

1 Introduction

In Lattice QCD the energy of a physical state is measured by studying the decay of correlators of operators which have a non-zero transition matrix element between the vacuum and the state under consideration. If the state is heavy, these correlators decay very fast in Euclidean time and one has to make sure that the temporal lattice spacing is small enough such that the signal of the correlator can be accurately traced over a few time slices before it disappears in the statistical noise. At the same time, one has to pay attention to choose the physical volume of the lattice large enough so that there are no significant finite-size effects. Both these requirements together lead to lattices with a large number of lattice sites and hence to computationally very expensive simulations. The obvious way out of this dilemma is to use a smaller lattice spacing in temporal direction compared to the spatial directions, i.e. the use of anisotropic lattices.

Anisotropic lattices have been widely used over the last few years. Studies comprising excited states of nucleons [1], heavy-quark bound states [2, 3, 4], heavy-light mesons [5, 6], heavy meson semi-leptonic decays [7], long range properties and excited states of the quark-antiquark potential [8, 9, 10, 11] as well as states composed purely of gluons (glueballs) [12, 13, 14, 15] or gluons and quarks (hybrids) [16, 17, 18, 19, 20, 21], have been performed, mainly using the standard anisotropic Wilson discretisation or a mean-link and Symanzik improved anisotropic action [22]. In fact, improved actions turned out to be crucial in anisotropic lattice calculations due to the coarse spatial lattice spacings employed. The discretisation of the continuum action, however, can be done in many different ways leading to different improvement schemes. A radical approach of improving lattice actions, based on Wilson's Renormalisation Group ideas, has been suggested by Hasenfratz and Niedermayer [23], namely the use of actions that are classically perfect, i.e. there are no lattice artifacts on the solutions of the lattice equations of motion. For SU(3) gauge theory the classically perfect FP action has been constructed and tested in [24, 25, 26, 27, 28] and the ansatz has been extended to include FP actions for fermions as well [29, 30, 31, 32, 33]. In the case of SU(2) gauge theory the FP action has been constructed in [34, 35, 36] and its classical properties have been tested on classical instanton solutions, both in SU(2) and SU(3) [37]. A classically perfect gauge action on anisotropic lattices, however, has so far been absent.

It is thus the goal of this work to fill the gap and to present the construction of classically perfect gauge actions on anisotropic lattices. The method has been introduced in [38] and it is presented in more detail in [39]. It relies upon a recent parametrisation of the isotropic classically perfect Fixed Point (FP) action [28, 40, 41] that includes a rich structure of operators as it is based on plaquettes built from simple gauge links as well as from smeared ("fat") links. We explicitly construct the $\xi = 2$ and 4 actions on coarse configurations typically occurring in Monte Carlo (MC) simulations. The properties of the $\xi = 2$ action are studied by performing measurements of the torelon dispersion relation (which serves for determining the renormalisation of the bare (input)

anisotropy), of the static quark-antiquark potential, of the deconfining phase transition and finally of the spectrum of low-lying glueballs in pure gauge theory.

It turns out that the construction of anisotropic classically perfect gauge actions is feasible. Measuring the renormalised anisotropy using the torelon dispersion relation turns out to be stable and unambiguous and shows that the renormalisation of the anisotropy is small and under good control. The measurements of the static quark-antiquark potential indicate that the violations of rotational symmetry are small if the (spatial) lattice is not exceptionally coarse. This shows that the parametrisation describes accurately the true classically perfect action, which is known to have good properties concerning rotational symmetry [27]. The study of the glueball spectrum is facilitated a lot due to the anisotropic nature of the action, even for (rather small) anisotropy $\xi = 2$. Results, including continuum extrapolations, are obtained for glueball states having much larger mass than the highest-lying states that could have been resolved with the same amount of computational work using the isotropic FP action. However, with the statistics reached so far, it is not yet possible to conclude whether the scaling properties of the glueball states, i.e. the behaviour of the measured energies as the lattice spacing is changed, are definitely better for the classically perfect action as compared to the mean-link and Symanzik improved anisotropic action [12, 13]. Especially, this is the case for the lowest-lying scalar glueball where the presence of a critical end point of a line of phase transitions in the fundamental-adjoint coupling plane, near the fundamental axis, causes large distortions of the scaling behaviour (sometimes called the “scalar dip”). Our action includes in its rich structure operators transforming according to the adjoint representation. If their coupling (which we do not control specifically during the construction and parametrisation) lies in a certain region, the effect of the critical end-point on scalar quantities at certain lattice spacings may even be enhanced compared to other (more standard) discretisations with purely fundamental operators. Concerning the lattice artifacts observed in the glueball simulations, we have to add that other effects, e.g. due to the finite size of the lattices, may also be present and that this issue requires further study. Being the first application of the FP action technique to anisotropic lattices, however, it goes beyond the scope of this work to systematically check all the possible sources of errors in the glueball mass determinations. Furthermore, we note that the computational overhead of the parametrised anisotropic classically perfect action compared to the standard Wilson action as well as to the mean-link and Symanzik improved action is considerable.

The paper is organised as follows. In section 2 we describe our method of generating anisotropic perfect gauge actions without having to perform a certain number of renormalisation group transformations (RGT) leading from very fine to coarse lattices typical for MC simulations. Instead, we make use of the parametrisation of the isotropic FP action presented in [28, 40, 41]. We start with the *isotropic* parametrised FP action on rather large fluctuations and perform a small number of purely *spatial* blocking steps. If a scale 2 block transformation is used, the resulting actions have anisotropies $\xi = 2, 4, 8, \dots$. The parametrisation ansatz used for these actions is a generalisation of the

isotropic parametrisation and is described as well.

Section 3 contains the main body of the present work, that is, the explicit construction and the application of a classically perfect gauge action on $\xi = 2$ anisotropic lattices. The results from measurements of physical quantities are presented there: the anisotropy of the action is measured using the torelon dispersion relation, the (spatial) scale is determined by the static quark-antiquark potential, where for some values of the coupling β , off-axis separations of the quarks are considered as well, in order to estimate violations of rotational symmetry by the parametrised action. Another way of determining the (temporal) scale is the study of the deconfining phase transition, measuring the critical couplings β_{crit} for different temporal extensions N_t of the lattice. Finally, the glueball spectrum is determined by performing simulations at three different lattice spacings using the $\xi = 2$ action and taking the continuum limits whenever it is possible.

The feasibility of iterating the procedure, i.e. adding one more spatial blocking step which leads to a classically perfect action with anisotropy $\xi = 4$, is briefly checked in section 4. It contains the explicit construction and parametrisation of the $\xi = 4$ action and the determination of the renormalised anisotropy via the torelon dispersion relation.

Section 5 finally contains a summary of the main results, some conclusions and an outlook to future work.

The parameters of the classically perfect actions used throughout this work are collected in appendix A, while appendix B contains the detailed results from our simulations.

2 The Construction of Perfect Anisotropic Actions

2.1 Introduction

The main idea for the construction of (effective) actions on anisotropic lattices is to start from an isotropic lattice and to perform one or more purely spatial renormalisation group transformations (RGT). Each scale two RGT step doubles the spatial lattice spacing but preserves the spacing in temporal direction. We are therefore naturally lead from an action on an isotropic lattice to (effective) actions on anisotropic lattices with anisotropies $\xi = 2, 4, 8, \dots$. Of course, choosing the scale s of the RGT different from two, we can in principle reach any desired anisotropy $\xi = s, s^2, s^3, \dots$.

A qualitative picture of the construction of classically perfect actions on anisotropic lattices is the following. We start from an isotropic FP action defined as a point in the infinite dimensional space of all couplings on the critical surface where the correlation length is infinite ($\beta \rightarrow \infty$). By performing one (or more) spatial RGT we move away from that point always staying on the critical surface. Since the spatial blocking kernel is zero on all classical configurations, the classical properties of the action are preserved exactly, i.e. it has no lattice

artifacts on the solutions of the (anisotropic) lattice equations of motion. (One can say that the action is an on-shell tree-level Symanzik improved action to all orders in a .) It is, however, important to note that the resulting anisotropic classically perfect (AICP) action is, generally speaking, no longer a FP action, i.e. the fixed point of a renormalization group transformation. However, it still possesses all the good properties of a classically perfect action, in particular it preserves scale invariant solutions of the classical equations of motion, i.e. classical instanton solutions. Moreover, since the spatial RGT steps are performed on the critical surface at $\beta \rightarrow \infty$, the transformation reduces to a saddle point problem representing an implicit equation for the anisotropic classically perfect action similar to the FP equation in the isotropic case.

In order to check whether this qualitative picture is correct and that the construction works in practice, we have analytically calculated the AICP actions for $d = 2$ scalar field theory (for earlier studies on this subject, see [42]) as well as for the quadratic approximation to $d = 4$ gauge theory for generic anisotropies ξ . In these two cases it turns out that starting from an anisotropic action for very smooth configurations and performing isotropic RGTs or starting from an isotropic FP action and performing an anisotropic RGT at the end is equivalent and leads to the same classically perfect anisotropic action. It also turns out that the quality of the results are as good as what has been obtained with the isotropic FP action [24, 27]. In particular we do not see any deviation from the classical continuum dispersion relation and almost no violation of the rotational symmetry in the perturbative potential for $r/a > 1$. For further details we refer to [39].

In practice the main advantage of applying one (or more) anisotropic spatial RGT is that we can directly start from a recent parametrisation of the isotropic FP gauge action [28, 40, 41] which is valid on rather coarse lattices. We can therefore avoid the cumbersome cascade procedure leading from very fine to coarser and coarser lattices.

In the following we first describe the anisotropic spatial blocking in section 2.2 and then present an extension of the isotropic parametrisation to include anisotropy in section 2.3.

2.2 The Spatial Blocking

The isotropic FP action is defined by the saddle point equation (at $\beta = \infty$):

$$\mathcal{A}^{\text{FP}}(V) = \min_{\{U\}} \{ \mathcal{A}^{\text{FP}}(U) + T(U, V) \}, \quad (1)$$

where $T(U, V)$ is the blocking kernel connecting the fine gauge configurations U to the coarse configurations V :

$$T(U, V) = \sum_{n_B, \mu} \left(\mathcal{N}_\mu^\infty(n_B) - \frac{k}{N} \text{Re} \text{Tr}[V_\mu(n_B) Q_\mu^\dagger(n_B; U)] \right), \quad (2)$$

where the normalisation term $\mathcal{N}_\mu^\infty(n_B)$ is given by

$$\mathcal{N}_\mu^\infty(n_B) = \max_{W \in \text{SU}(N)} \left\{ \frac{\kappa}{N} \text{Re Tr}[W Q_\mu^\dagger(n_B; U)] \right\}, \quad (3)$$

while $Q_\mu(n_B; U)$ is the blocked link,

$$Q_\mu(n_B; U) = W_\mu(2n_B; U) W_\mu(2n_B + \hat{\mu}; U). \quad (4)$$

Here $W_\mu(n; U)$ denotes a smeared (fuzzy) fine link, which is constructed as a sum of simple staples as well as of diagonal staples along the planar and spatial diagonal directions orthogonal to the link (RGT 3 transformation) [27], respectively.

To perform the blocking only spatially, doubling the lattice spacing in spatial direction while leaving the temporal lattice spacing unchanged, we use a purely spatial blocking kernel $T_{\text{sp}}(U, V)$ obtained by setting in the isotropic definition

$$Q_4(n_B; U) = W_4(2n_B; U) \quad (5)$$

thus doing only a smearing and no blocking in temporal direction. (In the case of spatial blocking the expression “ $2n_B$ ” stands for $(2n_B^1, 2n_B^2, 2n_B^3, n_B^4)$.) In addition, we have the freedom to choose different values of κ for the spatial (κ_s) and temporal (κ_t) blocking.

2.3 The Parametrisation

The classically perfect actions, described in principle by an infinite number of couplings, have to be parametrised in order to be suitable for numerical simulations. We have shown previously [28, 40, 41] that a parametrisation of the isotropic FP gauge action including APE-like smearing behaves much better and is much more flexible compared to common parametrisations using traces of closed loops with comparable computational cost. We thus decide to use an extension of this parametrisation to describe the anisotropic classically perfect gauge action.

For convenience, let us quickly review the parametrisation of the isotropic action. The parametrisation uses mixed polynomials of traces of simple loops (plaquettes) built from single gauge links $U_\mu(n)$ as well as from asymmetrically (APE-like) smeared links $W_\mu^{(\nu)}(n)$. We introduce the notation $S_\mu^{(\nu)}(n)$ for the sum of two staples of gauge links connecting two lattice sites in direction μ lying in the $\mu\nu$ -plane:

$$S_\mu^{(\nu)}(n) = U_\nu(n) U_\mu(n + \hat{\nu}) U_\nu^\dagger(n + \hat{\mu}) + U_\nu^\dagger(n - \hat{\nu}) U_\mu(n - \hat{\nu}) U_\nu(n - \hat{\nu} + \hat{\mu}). \quad (6)$$

To build a plaquette in a plane $\mu\nu$ from smeared links it is convenient to

introduce *asymmetrically* smeared links. First define²

$$Q_\mu^{(\nu)} = \frac{1}{4} \left(\sum_{\lambda \neq \mu, \nu} S_\mu^{(\lambda)} + \eta S_\mu^{(\nu)} \right) - \left(1 + \frac{1}{2} \eta \right) U_\mu. \quad (7)$$

Out of these sums of matrices connecting two neighboring points $n, n + \hat{\mu}$, we build the asymmetrically smeared links

$$W_\mu^{(\nu)} = U_\mu + \sum_{i=1} c_i Q_\mu^{(\nu)} (U_\mu^\dagger Q_\mu^{(\nu)})^{i-1}, \quad (8)$$

The parameters η, c_i used for the smearing may depend on local fluctuations measured by $x_\mu(n)$ defined as

$$x_\mu(n) = \text{Re Tr}(Q_\mu^s(n) U_\mu^\dagger(n)), \quad (9)$$

with the symmetrically smeared link

$$Q_\mu^s(n) = \frac{1}{6} \sum_{\lambda \neq \mu} S_\mu^{(\lambda)}(n) - U_\mu(n). \quad (10)$$

This parameter is negative, $-4.5 \leq x_\mu(n) \leq 0$, and it vanishes for trivial gauge configurations.

The smearing parameters are chosen to be polynomials of x_μ with free coefficients (determined later by a fit to the FP action):

$$\eta = \eta^{(0)} + \eta^{(1)} x + \eta^{(2)} x^2 + \dots, \quad (11)$$

$$c_i = c_i^{(0)} + c_i^{(1)} x + c_i^{(2)} x^2 + \dots. \quad (12)$$

Of course, the asymmetrically smeared links $W_\mu^{(\nu)}$ built out of a large number of paths connecting the neighbouring lattice sites are no longer elements of the SU(3) gauge group. They might be projected back to SU(3), however this task increases the computational cost in actual numerical simulations. Moreover, our studies have shown that projection reduces the degrees of freedom in defining the action and we are thus using the smeared links $W_\mu^{(\nu)}$ as they are.

We now build a smeared plaquette variable,

$$w_{\mu\nu} = \text{Re Tr}(1 - W_{\mu\nu}^{\text{pl}}), \quad (13)$$

as well as the ordinary one,

$$u_{\mu\nu} = \text{Re Tr}(1 - U_{\mu\nu}^{\text{pl}}), \quad (14)$$

where

$$W_{\mu\nu}^{\text{pl}}(n) = W_\mu^{(\nu)}(n) W_\nu^{(\mu)}(n + \hat{\mu}) W_\mu^{(\nu)\dagger}(n + \hat{\nu}) W_\nu^{(\mu)\dagger}(n) \quad (15)$$

²The argument n is suppressed in the following.

and

$$U_{\mu\nu}^{\text{pl}}(n) = U_\mu(n)U_\nu(n + \hat{\mu})U_\mu^\dagger(n + \hat{\nu})U_\nu^\dagger(n), \quad (16)$$

respectively. Finally, the action is built from these plaquette variables using a mixed polynomial ansatz of the form

$$\mathcal{A}[U] = \frac{1}{N_c} \sum_n \sum_{\mu < \nu} \sum_{k,l} p_{kl} u_{\mu\nu}(n)^k w_{\mu\nu}(n)^l, \quad (17)$$

where the coefficients p_{kl} are again free parameters defined by a fit to the FP action.

In order to adapt this parametrisation of the isotropic FP action to anisotropic actions, we use three (rather straightforward) extensions. Firstly, the coefficients p_{kl} in eq. (17) are chosen differently depending on the orientation of the plaquette $\mu\nu$, i.e., p_{kl}^{sp} for $\mu\nu \in \{12, 13, 23\}$ (spatial plaquettes) and p_{kl}^{tm} for $\mu\nu \in \{14, 24, 34\}$ (temporal plaquettes). Secondly, the parameter η entering in eq. (7) describing the asymmetry between differently oriented staples contributing to a smeared link $W_\mu^{(\nu)}$ is generalised to distinguish between smeared spatial and temporal links:

$$Q_i^{(j)} = \frac{1}{4} \left(\sum_{k \neq i,j} S_i^{(k)} + \eta_1 S_i^{(j)} + \eta_3 S_i^{(4)} \right) - \frac{1}{2} (1 + \eta_1 + \eta_3) U_i, \quad (18)$$

$$Q_i^{(4)} = \frac{1}{4} \left(\sum_{\lambda \neq i,4} S_i^{(\lambda)} + \eta_4 S_i^{(4)} \right) - \left(1 + \frac{1}{2} \eta_4 \right) U_i, \quad (19)$$

$$Q_4^{(j)} = \frac{1}{4} \left(\sum_{\lambda \neq 4,j} S_4^{(\lambda)} + \eta_2 S_4^{(j)} \right) - \left(1 + \frac{1}{2} \eta_2 \right) U_4, \quad (20)$$

where $i, j, k = 1, 2, 3$ and $\mu, \nu, \lambda = 1, \dots, 4$. The anisotropic parameters η_1, \dots, η_4 may be again polynomials in the local fluctuation parameter x_μ . These situations are depicted in Figure 1.

Finally, the construction of the smeared links $W_\mu^{(\nu)}$ from the matrices $Q_\mu^{(\nu)}$, described by the parameters c_i in eq. (8), is generalised such that these parameters are chosen differently for the construction of temporal links (always contributing to temporal plaquettes), spatial links contributing to spatial plaquettes and spatial links contributing to temporal plaquettes, c_{i1} , c_{i2} and c_{i3} , respectively, see Figure 2.

It is not a priori clear whether all the three extensions are necessary at the same time. Results from fits to different extended parametrisations (Table 2), however, show that it is indispensable to have the full parameter set. The values of χ^2 of the fit to the true classically perfect actions as well as the measured renormalised anisotropies of the parametrised action (see Section 3.2) indicate that the parametrisation is not flexible enough neither for $\eta_3 = \eta_4 \equiv 0$ (leading to a positive definite transfer matrix connecting only neighbouring time slices) nor if the parameters c_{ij} , $j = 1, 2, 3$ are set to be equal.

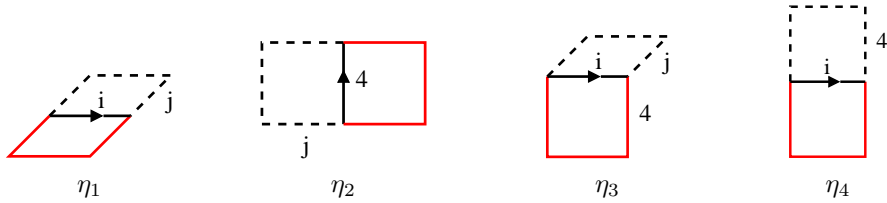


Figure 1: Asymmetry in the construction of the smeared link matrices $Q_\mu^{(\nu)}$. *From left to right:* spatial staple contributing to a smeared spatial link in a spatial plaquette (η_1), temporal staple contributing to a smeared temporal link (η_2), temporal staple contributing to a smeared spatial link in a spatial plaquette (η_3), temporal staple contributing to a smeared spatial link (η_4).

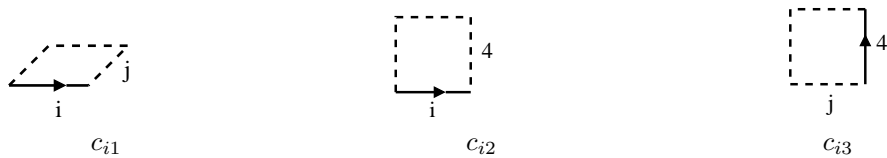


Figure 2: Asymmetry in the construction of the smeared links $W_\mu^{(\nu)}$ from the matrices $Q_\mu^{(\nu)}$. *From left to right:* spatial $Q_i^{(j)}$ contributing to a smeared spatial plaquette (c_{i1}), spatial $Q_i^{(4)}$ contributing to a smeared temporal plaquette (c_{i2}), temporal $Q_4^{(j)}$ (c_{i3}).

Our anisotropic action shall have the correct normalisation and anisotropy in the continuum limit. This can be accomplished by demanding the following two normalisation conditions to be exactly fulfilled [39]:

$$p_{01}^{\text{st}} + p_{10}^{\text{st}} + 2p_{01}^{\text{st}}c_{13} + p_{01}^{\text{st}}c_{13}\eta_2 + 2p_{01}^{\text{ss}}c_{11}\eta_3 + p_{01}^{\text{st}}c_{12}\eta_4 = \xi, \quad (21)$$

$$p_{01}^{\text{ss}} + p_{10}^{\text{ss}} + 2p_{01}^{\text{ss}}c_{11} + 2p_{01}^{\text{st}}c_{12} + 2p_{01}^{\text{ss}}c_{11}\eta_1 = \frac{1}{\xi}, \quad (22)$$

where all parameters η , c denote the constant (0th order) terms in the polynomials in x_μ .

Let us note that the parametrisation presented here leads to an overhead in the updates in MC simulations of 66 compared to the Wilson action and of 12 compared to the tadpole and tree-level improved action.

3 The $\xi = 2$ Perfect Action

# η	# c_i	n	$\max(k+l)_{\text{sp}}$	$\max(k+l)_{\text{tm}}$	χ_{d}^2	ξ_{R}
4	1	4	4	4	0.0250	1.63(2)
2	3	3	4	4	0.0238	
4	3	3	4	4	0.0144	1.912(9)

Table 1: Comparison of the accuracy χ_{d}^2 of the fit on derivatives on 20 configurations at $\beta = 3.5$ and the measured renormalised anisotropy ξ_{R} (using the torelon dispersion relation) at $\beta = 3.3$ for different choices of the set of non-linear parameters.

3.1 Construction

We construct the $\xi = 2$ classically perfect anisotropic action starting from the parametrised isotropic action [28] performing one spatial blocking step as described in Section 2. Studies of the quadratic approximation suggest $\kappa_t = \xi^2 \kappa_s = 4\kappa_s$ in the RG transformation for keeping the block transformation as close to the isotropic case as possible. Furthermore, spatial locality should stay at its optimum for the “isotropic” value of $\kappa_s = 8.8$ [27], thus we choose $\kappa_t = 35.2$. Indeed, it turns out that varying κ_t away from $\kappa_t = 35.2$, keeping $\kappa_s = 8.8$ fixed, makes it much more difficult to parametrise the resulting perfect action such that the renormalised anisotropy ξ_{R} stays close to the input value $\xi = 2$. Coarse configurations V are generated using the ad-hoc anisotropic action (see Appendix A.2), the FP eq. (1) including the purely spatial blocking kernel $T_{\text{sp}}(U, V)$ is used as a recursion relation with the intermediate isotropic action (see Appendix A.1) on the r.h.s. yielding the classically perfect $\xi = 2$ action on the l.h.s. Examining the blocking, we observe that coarse configurations obtained in a MC run with the ad-hoc anisotropic action are mapped to fine configurations that are close to isotropic (concerning spatial and temporal plaquette values and expectation values of the Landau gauge-fixed link variables) for input anisotropy $\xi_{\text{ad-hoc}} \approx 3.2$. We thus generate 20 configurations each at $\beta_{\text{ad-hoc}} = 2.5, 3.0, 3.5, 4.0$ using the ad-hoc anisotropic action³ with $\xi_{\text{ad-hoc}} = 3.2$. These configurations are spatially blocked using the intermediate isotropic action (see Appendix A.1) which describes the minimised isotropic configurations on the r.h.s. of eq. (1) reasonably well.

To construct the action, we perform several non-linear fits for the derivatives of 20 configurations at $\beta_{\text{ad-hoc}} = 3.5$, using different sets of parameters. The parameters c_i are chosen to be non-zero for $i = 1, 2, 3$ as adding additional free c_4 parameters does not improve χ^2 significantly.

³Note, that the values of $\beta_{\text{ad-hoc}}$, used in this section, may not be directly compared to the values of β_{perf} corresponding to the parametrised classically perfect action, used in the following sections; but rather the fluctuations (plaquette values, expectation values of Landau gauge-fixed links etc.) of the gauge configurations produced in MC runs using the perfect action should lie approximately in the same range as the fluctuations of the initial coarse configurations produced with the ad-hoc action.

Having fixed the non-linear parameters η and c_i , we include the derivatives of 20 configurations at $\beta_{\text{ad-hoc}} = 4.0$ and the action values of all the configurations at $\beta_{\text{ad-hoc}} = 3.5, 4.0$ in the linear fit of the parameters p_{kl} , keeping the non-linear parameters fixed. The resulting values of χ^2 and the linear behaviour of the actions suggest a linear set with $\max(k+l)_{\text{sp}} = 4$, $\max(k+l)_{\text{tm}} = 3$ where the action values are included with weights $w_{\text{act}} = 0.018$ relative to the derivatives. Using this value, the good parametrisation of the derivatives obtained in the full nonlinear fit is preserved, at the same time the mean error of the action value due to the parametrisation is as small as 0.35%. It is checked that the number of data points in the fit is large enough, making sure that the values of χ^2 as well as the errors of the action values do not increase significantly on configurations independent of those used in the fit. Furthermore, these quantities are determined on configurations down to $\beta_{\text{ad-hoc}} = 3.0$ and it turns out that the action works down to this value of $\beta_{\text{ad-hoc}}$. Finally, it is checked that the linear parameters p_{kl} do not lead to artificial gauge configurations in MC simulations caused by (local) negative contributions to the total action. The parameters of the resulting action are listed in Appendix A.3.

3.2 The Renormalised Anisotropy

The renormalised anisotropy ξ_R of the action presented above is measured using the torelon dispersion relation as described in [43, 44]. The torelon is a closed gluon flux tube encircling the periodic spatial boundary of size L of a torus. It is created and annihilated by closed gauge operators winding around this boundary. String models which are a good approximation for long flux tubes predict its energy to behave as

$$E(L) = \sigma L + \frac{\pi}{3L}, \quad (23)$$

where σ is the string tension and the second term describes the string fluctuation for a bosonic string [45, 46, 47, 48]. The string models assume no restriction on the transverse modes of the string, thus they apply to volumes with large transverse extension S . Due to this reason and because we prefer not to have too large transverse momenta, we work on $S^2 \times L \times T$ lattices, where S and T are large, whereas the length of the z -direction L is chosen to be rather short such that the torelon energy (see eq. (23)) is not too heavy. Since the colour flux tube has finite width in physical units, it is useful to employ (iteratively) APE smeared links [49] to improve the overlap of the operators with the ground state. One step of APE smearing acts on a spatial gauge link $U_j(x)$ as

$$\begin{aligned} \mathcal{S}_1 U_j(x) \equiv \mathcal{P}_{\text{SU}(3)} \left\{ U_j(x) + \lambda_s \sum_{k \neq j} (U_k(x) U_j(x + \hat{k}) U_k^\dagger(x + \hat{j}) \right. \\ \left. + U_k^\dagger(x - \hat{k}) U_j(x - \hat{k}) U_k(x - \hat{k} + \hat{j})) \right\}, \end{aligned} \quad (24)$$

the original link variable is replaced by itself plus a sum of the four neighbouring spatial staples and then projected back to SU(3). The smeared and projected

links $\mathcal{S}_1 U_j(x)$ have the same symmetry properties under gauge transformations, charge conjugation and reflections and permutations of the coordinate axes as the original gauge links. The smearing is used iteratively allowing to measure operators on different smearing levels, $\mathcal{S}_n U$.

We measure the operators

$$T_n(x, y, t) = \text{Tr} \prod_{z=0}^{L-1} \mathcal{S}_n U_z(x, y, z, t), \quad (25)$$

for all x, y, t , where $\mathcal{S}_n U_z$ is the n times iteratively smeared link in the longitudinal z direction. By discrete Fourier transform, we project out the state with momentum $\mathbf{p} = (p_x, p_y) = (n_x, n_y)(2\pi/Sa_s)$:

$$T_n(\mathbf{p}, t) = \sum_{x,y} T_n(x, y, t) e^{i(p_x x + p_y y)} \quad (26)$$

and build the correlators

$$C_{nn'}(\mathbf{p}, t) = \frac{1}{N_t} \sum_{\tau} \langle T_n(\mathbf{p}, \tau) T_{n'}(-\mathbf{p}, \tau + t) \rangle. \quad (27)$$

From these correlators of operators measured on the different smearing levels we obtain the energy values $a_t E(\mathbf{p})$ using variational methods (see Appendix B of [28]). The continuum dispersion relation

$$E^2 = \mathbf{p}^2 + m^2 \quad (28)$$

on the lattice becomes (in temporal units)

$$(a_t E)^2 = a_t^2 (\mathbf{p}^2 + m^2) = \frac{(a_s \mathbf{p})^2}{\xi_R^2} + (ma_t)^2 = \frac{1}{\xi_R^2} (n_x^2 + n_y^2) \left(\frac{2\pi}{S} \right)^2 + (ma_t)^2, \quad (29)$$

where n_x, n_y are the components of the (transversal) lattice momentum. On an anisotropic lattice, this equation allows for the extraction of the renormalised anisotropy $\xi_R = a_s/a_t$ (measuring the “renormalisation of the speed of light”) as well as the torelon mass ma_t , which in turn may be used to get an estimate of the scale using eq. (23) and known values of the string tension σ . The main advantage of this approach is obtaining the renormalised anisotropy ξ_R as well as an estimate for the scales a_s and a_t by performing computationally rather inexpensive measurements.

The parameters of the simulations carried out are collected in Table 2.

The Polyakov line around the short spatial direction is measured using operators at smearing levels $\mathcal{S}_n U$ with $n = 3, 6, 9, 12, 15$ for $\beta \geq 3.3$ and $n = 2, 4, 6, 8, 10$ for $\beta \leq 3.15$, respectively, and smearing parameter $\lambda_s = 0.1$. The measured energies $E(p^2)$ are given, together with the number of operators used in the variational method, the fit ranges and the values of χ^2 per degree of freedom, χ^2/N_{DF} , in Tables 24 and 25 in Appendix B.

β	$S^2 \times L \times T$	# sweeps / measurements
3.00	$8^2 \times 4 \times 20$	72000 / 14400
3.15 ^a	$8^2 \times 5 \times 20$	54000 / 10800
3.15 ^b	$5^2 \times 8 \times 20$	47600 / 9520
3.30	$12^2 \times 6 \times 30$	35600 / 7120
3.50 ^a	$12^2 \times 8 \times 24$	39400 / 7880
3.50 ^b	$14^2 \times 6 \times 30$	36800 / 7360

Table 2: Run parameters for the torelon measurements using the $\xi = 2$ perfect action. The lattice extensions in torelon direction L , the extension in the two transversal spatial directions S as well as the temporal extension T are given.

Figure 3 displays an example of a dispersion relation at $\beta = 3.3$ including all values of p at which the energies could be determined on the given lattice. Note, that the energies of the $p = 0$ torelons (the torelon masses) may be hard to determine because the effective masses do not reach a plateau within the temporal extent of the lattice, probably due to the small overlap of the operators used with these states; however, using the non-zero momentum energies, the masses may still be accurately determined.

To determine the renormalised anisotropy ξ_R as well as the torelon mass in units of the temporal lattice spacing ma_t , we perform fits to the dispersion relation, taking into account the correlations between different operators. The range of p^2 considered is chosen depending on χ^2/N_{DF} of the fit and the precision of the dispersion relation data in the respective range. The results are given in Table 3.

β	fit range	ξ_R	$m_{\text{T}}a_t$	χ^2/N_{DF}
3.00	0..5	1.903(81)	1.324(98)	0.39
3.15 ^a	0..4	1.966(39)	0.700(35)	0.83
3.15 ^b	0..5	2.022(104)	1.262(84)	0.62
3.30	1..9	1.912(9)	0.311(5)	0.94
3.50 ^a	1..10	1.836(9)	0.149(10)	0.94
3.50 ^b	1..8	1.826(16)	0.208(16)	1.61

Table 3: Results of the torelon simulations using the $\xi = 2$ perfect action. The fit range in p^2 is given in units of $(2\pi/S)^2$.

Using the finite size relation for the torelon mass corresponding to eq. (23),

$$M_T(La_s) = \left(\sigma + \frac{D}{(La_s)^2}\right)La_s, \quad (30)$$

we calculate the string tension σ and thus the spatial scale a_s . The string model predicts $D = -\frac{\pi}{3}$ for long strings thence we use this string picture value and stay aware that the estimate gets worse for short strings. To obtain the hadronic scale r_0 and the lattice spacings we employ $r_0\sqrt{\sigma}=1.193(10)$ from [28] and use the definition $r_0 = 0.50$ fm. The results are collected in Table 4.

The two simulations denoted by 3.15^b and 3.50^b are used to check the stability of the method. The first one is carried out on a lattice with small transversal spatial size (the torelon string measured is even longer), the latter is measuring the energies of a rather short string. The scale is measured accurately using the static quark-antiquark potential (see Section 3.3.1) so that we can compare our torelon estimates to the much more reliable values in Table 5. It turns out that the deviation of the torelon estimates for the scale r_0/a_s from the potential values does not exceed 6% if the length of the string is not too short (say $La_s \gtrsim 1$ fm). For short strings, the string picture does not apply and we may therefore not expect good results in this case. But even for very long strings, it is not possible to obtain very accurate information about the scale as long strings are very heavy and thus difficult to measure (comparable to the long range region of the static quark-antiquark potential), especially when the anisotropy ξ is not very large.

There seems to be no problem if the transverse volume is rather small as in the $\beta = 3.15^b$ simulation, except of course the large momenta occurring which make the determination of the energies more difficult. As well, the estimates of the renormalised anisotropy ξ_R do not show significant deviations neither for small transverse volume nor for short strings.

β	$\sqrt{\sigma}a_s$	r_0/a_s	a_s [fm]	a_t [fm]
3.00	0.834(20)	1.43(5)	0.350(12)	0.184(14)
3.15 ^a	0.563(8)	2.12(5)	0.236(6)	0.120(5)
3.15 ^b	0.579(18)	2.06(8)	0.243(9)	0.120(11)
3.30	0.3578(21)	3.33(5)	0.150(2)	0.079(1)
3.50 ^a	0.225(5)	5.31(16)	0.094(3)	0.051(2)
3.50 ^b	0.304(7)	3.92(12)	0.128(4)	0.070(3)

Table 4: Estimates of the scale determined from torelon results (see Table 3), see text.

Finally, we may conclude that determining the renormalised anisotropy using the torelon dispersion relation is a stable and apparently sensible procedure. There are no manifest problems and it works on fine lattices as well as on

β	La_s [fm]	r_0/a_s (Torelon)	r_0/a_s (Potential)	rel. error
3.00	1.48	1.43(5)	1.353(16)	+5.7%
3.15 ^a	1.23	2.12(5)	2.038(2)	+4.0%
3.15 ^b	1.96	2.06(8)	2.038(2)	+1.1%
3.30	0.95	3.33(5)	3.154(8)	+5.6%
3.50 ^a	0.82	5.31(16)	4.906(21)	+8.2%
3.50 ^b	0.61	3.92(12)	4.906(21)	-20.0%

Table 5: The estimates of the scale obtained from torelon measurements (see Table 4) compared to the scale measured using the static quark-antiquark potential (see Table 8). The length of the torelon string La_s in physical units is given as well.

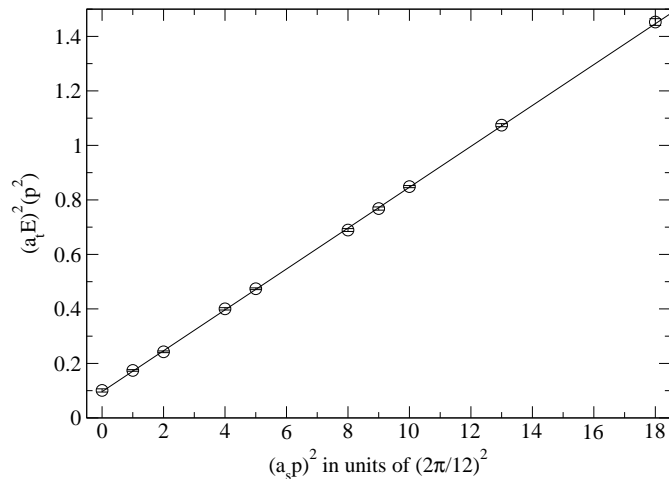


Figure 3: Torelon dispersion relation for $\beta = 3.3$. The straight line is the correlated fit to $E^2(p) = m_T^2 + p^2$ in the range $p^2 = 1..9$.

coarse ones. Checks employing different lattice extensions indicate that the determination of the renormalised anisotropy is quite stable within a large range of different choices. The estimate of the lattice scale, however, is not very accurate, mainly due to the use of the string picture relation, eq. (30); the (systematic) error of the torelon scale is about 5% for reasonable torelon lengths $L \gtrsim 1$ fm with a tendency of underestimating the lattice spacing a_s .

3.3 The static quark-antiquark potential

3.3.1 The Scale

To set the scale of the action at a given β -value we measure the static quark-antiquark potential, which is reasonably well described by the phenomenological ansatz [50],

$$V(R) = V_0 + \frac{\alpha}{R} + \sigma R. \quad (31)$$

We determine the lattice spacing using the following definition of r_c [51]:

$$r^2 V'(r)|_{r=r_c} = c, \quad (32)$$

where the well-known Sommer scale $r_0 \approx 0.50$ fm corresponds to $c = 1.65$. For the anisotropic action, we employ the conventional definition of r_0 , however, $V(r)$ is now measured in units of the temporal lattice spacing and thus we have

$$-\alpha + \xi \hat{\sigma} \left(\frac{r_c}{a_s}\right)^2 = c, \quad (33)$$

where $\hat{\sigma}$ denotes the fitted dimensionless value $\hat{\sigma} = \sigma a_s a_t$ of the string tension. The renormalised anisotropy ξ thus has to be known before the spatial scale r_0 may be determined. For very fine or coarse lattices it may be advantageous to go to a slightly different separation corresponding to a different value of the constant c on the r.h.s. For this purpose, we have collected values for c and r_c from high-precision measurements of the static potential performed with the Wilson action [52, 53, 54] listed in Table 6.

r_c/r_0	c
0.662(1)	0.89
1.00	1.65
1.65(1)	4.00
2.04(2)	6.00

Table 6: Parameter values for the determination of the hadronic scale r_c through $r^2 V'(r)|_{r=r_c} = c$.

The static quark-antiquark potential is measured on lattices of different scales $a_s = 0.10 \dots 0.37$ fm, employing Wilson loops built out of APE smeared

(see Section 3.2) spatial links and simple temporal gauge links. The measurements at $\beta = 3.00, 3.30$ include the determination of the potential between quarks that are off-axis separated along the lattice vectors $(1,0,0)$, $(1,1,0)$, $(1,1,1)$, $(2,1,0)$, $(2,1,1)$, $(2,2,1)$ (and lattice rotations thereof) in order to estimate violations of rotational symmetry. The rest of the measurements include only on-axis separations due to the large computational cost (concerning speed and memory) of the off-axis measurement. The smearing levels used are as follows ($\lambda_f = 0.1$ on all the lattices): on the finest lattice at $\beta = 3.50$, we use $\mathcal{S}_n U, n = 3, 6, 9, 12, 15$; at $\beta = 3.15$ we use $\mathcal{S}_n U, n = 2, 4, 6, 8, 10$; for the measurements including off-axis separations, we employ only three different smearing levels each, in order to save memory and time: $\mathcal{S}_n U, n = 5, 10, 15$ at $\beta = 3.30$ and $\mathcal{S}_n U, n = 2, 4, 6$ on the coarsest lattice at $\beta = 3.00$. The parameters of the simulations are given in Table 7.

β	off-axis sep.	$S^3 \times T$	# sweeps / measurements
3.00	yes	$8^3 \times 16$	42000 / 2800
3.15	no	$10^3 \times 20$	39800 / 3980
3.30	yes	$10^3 \times 20$	27000 / 1800
3.50	no	$12^3 \times 24$	36400 / 3640

Table 7: Run parameters for the measurements of the static quark-antiquark potential using the $\xi = 2$ perfect action.

The values of the off-axis potential $a_t V(\vec{r})$ at $\beta = 3.30$ are collected in Table 26 in Appendix B and displayed in Figure 4, the values of the off-axis potential on the coarse lattice at $\beta = 3.00$ are collected in Table 27. The potential values $a_t V(r)$ of the on-axis simulations are collected in Table 28.

The parameters α and σ (the string tension) in the phenomenological potential ansatz, eq. (31), are determined using global fits, the hadronic scale r_0 is determined performing local fits. The fit ranges and results are given in Table 8. In the global fit to the off-axis potential at $\beta = 3.30$ we exclude the badly measured separations $2(2, 1, 0)$ and $2(2, 1, 1)$.

In principle, it is possible to determine the renormalised anisotropy using the first excited state of the potential together with the ground state. The ground state values are again fitted to the ansatz $V(r) = V_0 + \alpha/r + \sigma r$, whereas the values of the excited state are fitted to the (ad-hoc) ansatz $V^*(r) = A/r + B + Cr + Dr^2$. As can be seen from Figure 5, however, for the off-axis potential at $\beta = 3.3$, the energy values of the first excited state have large errors. The result for the separation $a_t(V^*(r_0) - V(r_0)) = 0.555(47)$ thus shows a large error. Comparing this value to $r_0(V^*(r_0) - V(r_0)) \approx 3.25(5)$ of [55] one obtains $\frac{r_0}{a_t} = 5.86(59)$ and thus $\xi_R = a_s/a_t = 1.86(19)$ for $\beta = 3.3$ which is in agreement with the value determined using the torelon dispersion relation, $\xi_R = 1.912(9)$. A similar determination for the on-axis potential at $\beta = 3.50$ is even more difficult due to the smaller number of separations measured. The result is $\xi_R = 1.66(32)$

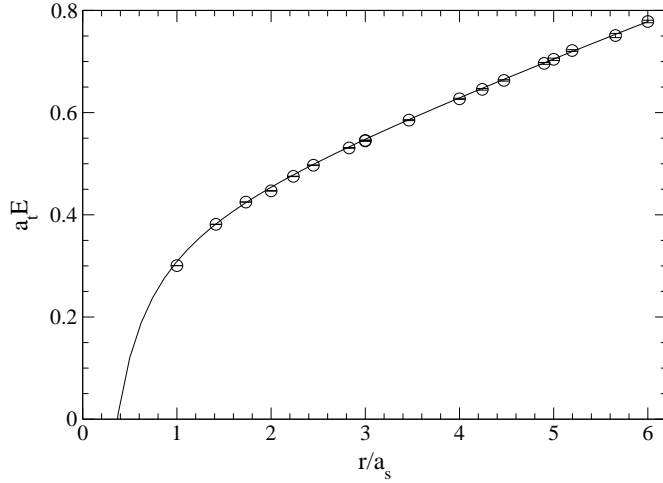


Figure 4: Ground state of the static quark-antiquark potential at $\beta = 3.3$. Including a fit to the phenomenological potential ansatz in the range $r = \sqrt{2}..5$.

β	gl. fit	α	$\sigma a_s a_t$	loc. fit	r_0/a_s	$r_0\sqrt{\sigma}$
3.00	$1 - 2\sqrt{6}$	-0.201(18)	0.3595(87)	$\sqrt{6} - 3$	1.353(16)	1.119(51)
3.15	$1 - 5$	-0.1503(12)	0.1654(6)	$1 - 3$	2.038(2)	1.162(15)
3.30	$\sqrt{2} - 5$	-0.1539(7)	0.0683(3)	$2\sqrt{2} - 2\sqrt{3}$	3.154(9)	1.140(8)
3.50	$1 - 6$	-0.1478(4)	0.0320(3)	$2 - 4$	4.906(21)	1.189(14)

Table 8: Results of the measurements of the static quark-antiquark potential using the $\xi = 2$ perfect action. The parameters α and σ of the potential ansatz eq. (31) are given together with the global fit range chosen to determine them. The hadronic scale r_0 is given in spatial lattice units together with the local fit range used to determine that quantity. Note, that we have chosen $c = 6.00$ and $c = 0.89$ for $\beta = 3.0$ and $\beta = 3.5$, respectively (see Section 3.3.1). Additionally, the dimensionless quantity $r_0\sqrt{\sigma}$ is given.

which does again agree with the torelon result, $\xi_R = 1.836(9)$. Due to the large errors (possibly caused by the operators used, optimised for the ground state) this method of determining the renormalised anisotropy ξ_R is not suitable in the context of this work. However, for the determination of the scale as well as of the anisotropy on lattices with finer temporal lattice spacing (above all with higher anisotropies) this way might be feasible at least if off-axis separations are included in the measurement.

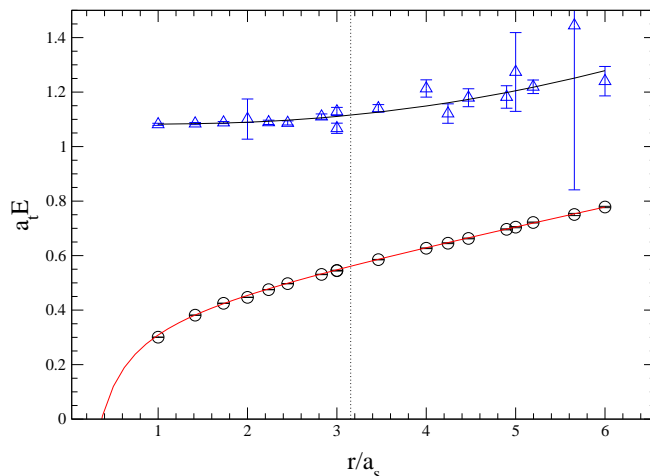


Figure 5: Static quark antiquark potential at $\beta = 3.3$ including the first excited state $V^*(r)$ at $\beta = 3.3$. The location of r_0 where the determination of the anisotropy is done, using the gap, is marked by the dotted line.

3.3.2 Rotational invariance and scaling

The measurements at $\beta = 3.0, 3.3$ including a large number of off-axis separations provide information about the deviations from rotational invariance. This issue has been addressed in [27] for the RGT used in this work and it turned out that violations of rotational symmetry caused by the blocking are small. That this is still true for the parametrisation employed here is shown by the off-axis potential at $\beta = 3.30$, see Figure 4. The deviations on the coarse lattice at $\beta = 3.00$ are significantly larger (see Figure 6) which is no surprise as this coupling corresponds to a spatial lattice spacing $a_s \approx 0.37$ fm. We present some dimensionless ratios containing information about the deviation from rotational invariance in Tab. 9; due to the resulting small values the errors are rather large. One notices that the parametrised perfect action does a good job, for

$\beta = 3.30$ the deviation between the exactly degenerate separations (2,2,1) and (3,0,0) is zero (within statistical errors).

β	$\frac{V(1,1,1)-V_{\text{fit}}(\sqrt{3})}{V(2,0,0)-V(1,0,0)}$	$\frac{V(2,2,1)-V(3,0,0)}{V(3,0,0)-V(1,0,0)}$
3.00	0.086(4)	0.057(6)
3.30	0.029(7)	0.005(6)

Table 9: The normalised deviations from rotational invariance for the AICP action. The ratios displayed are zero in the case of no rotational symmetry violation.

The static $q\bar{q}$ -potential is also an effective test of scaling. Expressing the potential measurements performed at different couplings β in the RG invariant, dimensionless ratios r/r_0 and r_0V and subtracting the unphysical constant $r_0V(r_0)$ should lead to potentials lying exactly on top of each other. Deviations indicate either scaling violations or ambiguities in the determination of r_0 . Figure 6 includes all potential measurements and shows that the different curves can hardly be distinguished from each other, except some energies determined on the coarsest lattice at $\beta = 3.00$. They deviate notably from the curve which is a fit to the phenomenological potential ansatz, eq. (31), including all the measurements that have been included into the global fits of the single β values, see Table 8. The results for the two physical parameters from this global fit are $\alpha = -0.27799(5)$ and $\sigma r_0^2 = 1.3690(3)$.

3.4 The Critical Temperature

The critical temperature of the deconfining phase transition contains information about the temporal scale of the lattice at a given coupling β as $T_c = 1/(N_t a_t)$. Comparing this information to quantities obtained from the measurements of torelons or the static quark-antiquark potential offers many interesting scaling (and other) tests. However, since measurements of such quantities at the determined values of β_{crit} are yet absent and because interpolations in β are very difficult due to the renormalisation of the anisotropy ξ , these tests are a future project.

The critical temperature T_c may be defined as the location of the peak in the susceptibility of the Polyakov loop P (Wilson line in temporal direction),

$$\chi \equiv N_s^3 (\langle |P|^2 \rangle - \langle |P| \rangle^2). \quad (34)$$

We determine the values of $\beta_c(N_t)$ on rather coarse lattices with temporal extensions $N_t = 3, \dots, 7$. Simulations at different values of β near the estimated critical couplings β_c are performed and the peaks are determined by employing the Ferrenberg-Swendsen multi-histogram reweighting [56, 57] (see also [40, 28, 39] for additional details). The run parameters of the simulations are collected in Table 10.

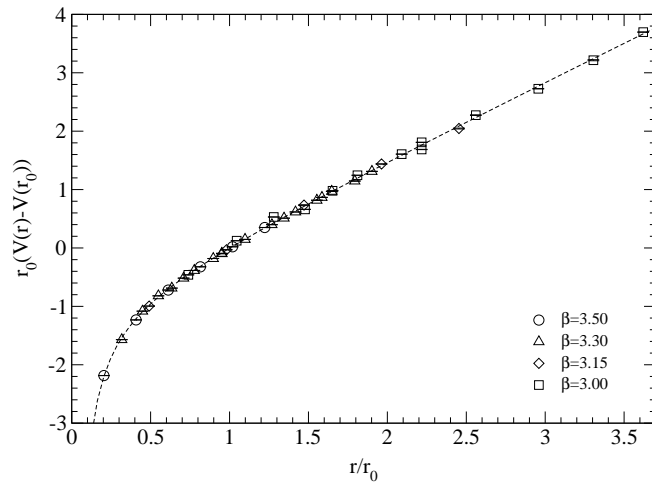


Figure 6: The static quark-antiquark potential measurements expressed in RG invariant, dimensionless units r/r_0 , r_0V . The unphysical constant $r_0V(r_0)$ has been subtracted such that all the curves exactly coincide at $r = r_0$. The dashed line is a global fit to the phenomenological potential ansatz, eq. (31).

In this first study, we decide not to examine the finite-size scaling of β_{crit} but to choose $L_s/L_t = \xi \cdot N_s/N_t \approx 3.5 \sim 4$. Obviously, the anisotropic nature of the action makes the computational effort of the simulations for exploring the deconfining phase transition smaller. The effects of the finite volume are (rather conservatively) estimated by using the finite-size scaling relation for a first order phase transition,

$$\beta_c(N_t, N_s) = \beta_c(N_t, \infty) - h \left(\frac{N_t}{N_s} \right)^3. \quad (35)$$

The parameter $|h|$ is set to the largest value $|h| = 0.25$ that has been observed with the isotropic action, and the value of ξ_R used to estimate the spatial lattice volume is set to the lowest value appearing in the whole range of β values considered. The extrapolated critical couplings β_c are given together with the statistical error and the estimated finite-volume error in the last column of Table 10.

3.5 Glueballs

3.5.1 Introduction

The particles mediating the strong interaction of QCD, the gluons, carry colour charge and thus interact with each other, unlike, e.g., their counterpart in electromagnetism, the photons, which have zero electric charge. The spectrum of QCD may thus contain bound states of (mainly) gluons, called glueballs. These states are described by the quantum numbers J denoting the (integer) spin, P denoting the eigenvalue ± 1 of the state under parity and C denoting the eigenvalue ± 1 under charge conjugation. Thus the eigenstates of the Hamiltonian corresponding to glueball states are labeled $|J^{PC}\rangle$.

Currently, there is an ongoing debate whether light glueballs (above all the scalar 0^{++} which is the lightest state in pure lattice gauge theory with a mass of about 1.6 GeV) have been observed experimentally at about the mass that is predicted by quenched simulations on the lattice, whether the lightest glueball is much lighter (below 1 GeV) and very broad [58], or whether glueballs have not been observed at all in experiments [59]. There are mainly two reasons for this uncertainty. On one hand, the experimental data seem not yet to be accurate and complete enough, despite large efforts in the last years, driven by the lattice results; on the other hand, lattice simulations with high statistics, measuring glueball states, have been performed only in the quenched approximation, where the quarks are infinitely heavy and thus static. Decreasing the sea (dynamical) quark mass (finally down to the physical value) will allow to track the glueball states as sea quark effects are increased. It may turn out, that indeed the glueball mass is lighter than the one measured in pure gauge theory (for partially quenched results possibly indicating this see [60, 61, 62]). It may even happen that by “switching on” the sea quarks the scalar glueball starts to decay (almost) instantaneously to $q\bar{q}$ states, i.e. it ceases to exist physically. However, the (partially) unquenched results are rather indecisive yet.

lattice size	β	sweeps	τ_p	τ_{int}	χ_L	β_c
3×6^3	2.80	45000		70	1.45(5)	2.863(1)(5)
	2.85	45000	410	259	11.3(20)	
	2.87	45000		312	21.6(28)	
	2.90	50000		100	2.34(10)	
4×8^3	3.00	45000		81	1.63(5)	3.032(1)(5)
	3.02	45000	870	102	3.97(26)	
	3.03	45000	830	372	43.2(22)	
	3.04	45000		188	10.9(18)	
	3.05	55600		144	3.94(21)	
5×9^3	3.07	44000		117	0.84(4)	3.118(1)(6)
	3.10	45000	560	154	4.38(63)	
	3.11	20500	640	198	15.0(27)	
	3.12	44500	3700	278	33.2(19)	
	3.15	20000		110	3.26(18)	
6×11^3	3.17	45000	1440	121	7.4(11)	3.181(1)(6)
	3.18	45000	1750	201	30.0(15)	
	3.185	45000		232	23.2(24)	
	3.19	45000		123	10.4(14)	
	3.20	45000		100	5.62(36)	
7×13^3	3.22	32400	700	87	6.7(5)	3.236(1)(6)
	3.23	44500	750	129	18.4(11)	
	3.24	29000		149	20.7(16)	
	3.25	22400		83	9.2(10)	

Table 10: Run-time parameters of $\xi = 2 T_c$ -simulations. The number of sweeps, the persistence time τ_p (if applicable), the integrated autocorrelation time τ_{int} and the Polyakov loop susceptibility χ_L are given for all values of β used in the final reweighting procedure, as well as the resulting β_c . The systematic error in the second brackets is a (rather conservative) estimate of the finite volume effects and has to be considered if the given value should be an estimate of the infinite-volume critical coupling.

Γ^p	D_0	D_1	D_2	D_3	D_4	D_5	D_6
A_1	1	0	0	0	1	0	1
A_2	0	0	0	1	0	0	1
E	0	0	1	0	1	1	1
T_1	0	1	0	1	1	2	1
T_2	0	0	1	1	1	1	2

Table 11: The composition of the subduced representation $D_J \downarrow O_h$ in terms of the irreducible representations of the cubic group O_h .

3.5.2 Glueballs on the Lattice

Glueballs in the continuum are rotationally invariant and have a certain (integer) spin J . On the lattice, the rotational $O(3)$ symmetry is broken, only its discrete cubic subgroup O_h survives the discretisation. Therefore, the eigenstates of the transfer matrix are classified according to the five irreducible representations of O_h : A_1 , A_2 , E , T_1 , T_2 with dimensions 1, 1, 2, 3, 3 respectively. Their transformation properties may be described by polynomials in the components x, y, z of an $O(3)$ vector as follows: $A_1 \sim \{1\}$, $A_2 \sim \{xyz\}$, $E \sim \{x^2 - z^2, y^2 - z^2\}$, $T_1 \sim \{x, y, z\}$, $T_2 \sim \{xy, xz, yz\}$. Generally, an $O(3)$ representation with spin J splits into several representations of the cubic group. Since O_h is a subgroup of $O(3)$, any representation D_J with spin J in the continuum induces a so-called subduced representation $D_J \downarrow O_h$ on the lattice. This subduced representation no longer has to be irreducible but is a direct sum of irreducible representations Γ^p of O_h :

$$D_J \downarrow O_h = \Gamma^1 \oplus \Gamma^2 \oplus \dots \quad (36)$$

Table 11 lists the subduced representations of D_J for $J = 1, \dots, 6$. The spin $J = 2$ state for example splits up into the 2-dimensional representation E and the 3-dimensional representation T_2 . Approaching the continuum, rotational symmetry is expected to be restored and thus, as a consequence the mass splitting of these two states will disappear and the two representations form together the 5 states of a spin $J = 2$ object.

Pure glue physical states on the lattice are created and annihilated by applying gauge invariant operators to the pure gauge vacuum. In our simulations, we use space-like Wilson loops in the fundamental representation of $SU(3)$. Since we do not aim at measuring non-zero momentum glueballs we consider only translationally invariant operators, i.e. operators averaged in space.

It is computationally feasible to measure Wilson loop operators up to length 8. The composition of the irreducible representations Γ^{PC} of the cubic group in terms of these 22 loop shapes has been done already in Ref. [63]. Operators contribute to the two- and three-dimensional representations with two and three

different polarisations, respectively, in analogy to different magnetic quantum numbers m for a given angular momentum l in the $O(3)$ group. Measuring all these polarisations may suppress statistical noise more than just increasing statistics since the different polarisations of a loop shape are expected to be anti-correlated.

Due to mixing with other states present in pure gauge theory on a periodic lattice, such as torelons or glueball pairs, and due to the breaking of the continuum rotational symmetry by the lattice, the identification and the continuum spin assignment of single glueball states are additional vital questions which will be addressed in Sections 3.5.5, 3.5.7.

3.5.3 Simulation Parameters

To allow for a continuum extrapolation, at least for the lighter states, we decide to perform simulations at three different lattice spacings in the range $0.10 \text{ fm} \leq a_s \leq 0.25 \text{ fm}$ in volumes between $(1.2 \text{ fm})^3$ and $(2.0 \text{ fm})^3$. The simulation parameters are given in Table 12. The gauge fields are updated by performing compound sweeps consisting of 4 pseudo over-relaxation and 1 Metropolis sweep, and after every 2 compound sweeps we measure all 22 loop shapes up to length 8. The measurement is performed on APE-smearred configurations (see Section 3.2) in order to spatially enlarge the operators, thus improving the overlap with the glueball states and reducing unphysical high-momentum fluctuations. On the coarse lattice at $\beta = 3.15$ we use smearing levels $\mathcal{S}_n, n = 2, 4, 6, 8, 10$, on the other lattices we use levels $\mathcal{S}_n, n = 3, 6, 9, 12, 15$, always with smearing parameter $\lambda_s = 0.1$.

β	$(a_s/r_0)^2$	$S^3 \times T$	V	# sweeps / measurements
3.15	0.2408(5)	$8^3 \times 16$	$(1.96 \text{ fm})^3$	241000 / 24100
3.30	0.1005(6)	$10^3 \times 20$	$(1.59 \text{ fm})^3$	99000 / 9900
3.50	0.0415(4)	$12^3 \times 24$	$(1.22 \text{ fm})^3$	115000 / 11500

Table 12: Run parameters for the glueball simulations using the $\xi = 2$ perfect action.

3.5.4 Determination of the Energies

The masses of the lowest states and the first excited states (if possible) in all the representations are determined using the variational techniques described in Appendix B of [28]. The results in units of the temporal lattice spacing a_t are listed in Tables 29 – 31 in Appendix B together with the number N of operators entering into the fitting procedure, the time slices on which the initial generalised eigenvalue problem is solved (usually 1/2), the number of operators M in the final fit and the corresponding value of χ^2/N_{DF} . These results are

then multiplied by $\xi_R \cdot r_0/a_s$ from Tables 3 and 8 to obtain the glueball masses in units of the hadronic scale r_0 , listed in Table 13.

In order to obtain reliable estimates of the glueball masses from the variational method, one has to pay attention that among the large number of operators (up to 145 from five smearing levels) there are no correlators entering the process that are measured exceptionally bad, i.e. with large errors even at small time separation, as this may destabilise the determination. To filter out such data, we look at the relative errors of the single operators depending on the temporal separation of the creation and annihilation operators and drop all correlators whose signal falls below a certain threshold value. Usually, this is repeated with different threshold values, yielding different sized sets of operators (2 ~ 4 sets per representation). We perform $O(100)$ mass determinations on each operator set, varying the analysis parameters such as M (see Appendix B of [28]) or the fitting range $t = t_{\min} \dots t_{\max}$. It turns out that generally the variational method used is stable, provided that the badly measured operators are absent from the beginning and provided that no important operators are missing. Patently, to find such a window of the number of initial operators, N , may be difficult if there is a rather small total number of operators.

For some of the heavy states, such as the $PC = --$ glueballs, whose masses can only be determined from the $\beta = 3.50$ measurements, we have to resort to using the correlators at $t_0 = 0$ and $t_1 = 1$ for the solution of the first generalised eigenvalue problem. This has the advantage that the correlators from separation $t_0 = 0$ are positive definite by definition (which is not true for $t_0 \geq 1$), thus rendering the second generalised eigenvalue problem well defined even if all the initial operators are kept, $M = N$. However, the correlators $C(t = 0)$ are under suspicion of containing rather little physical information about the correlation lengths (which correspond to the *decay* of the correlators), actually they almost only provide information about the relative normalisation of operators. Obviously, operators with a large signal at $t = 0$ might be preferable because their signal/noise ratio is probably better on average, however in general they do not correspond to the operators having the largest overlap with the lowest-lying states. It turns out that one has to pay much more attention in choosing the fit range $t = t_{\min} \dots t_{\max}$ when using $t_0 = 0$, $t_1 = 1$ because in this case at small t the contamination of the lowest masses due to higher states is much more significant.

During the analysis, it turns out that the mass determinations for the scalar representation A_1^{++} are rather challenging. The ground state receives a larger relative error than comparable states where the operators are measured equally well; for the first excited state it is very hard to obtain a stable determination, and the error of its mass may turn out to be huge (e.g. at $\beta = 3.50$). Probably, it is the underlying vacuum, having the same quantum numbers as the glueball state, that is responsible for these troubles. We treat the vacuum just like another state in this representation, so that the glueball ground state is effectively a first excited state and the glueball first excited state is effectively a second excited state of the representation. Attempts of using other ways of getting rid of the vacuum such as the usual v.e.v. subtraction or the subtraction of large t

correlators (that are assumed to contain solely noise, however correlated to the noise at lower t) or even more sophisticated methods (like solving a generalised eigenvalue problem using large t correlators to dig out the vacuum state) do not at all succeed in improving the situation.

3.5.5 Torelons and Multi-Glueball States

Besides single glueballs, the spectrum of pure gauge theory on a lattice with periodic boundary conditions also contains states consisting of several glueballs, torelons or mixed states of glueballs and torelons. Although we expect that the operators used to measure glueball energies couple most strongly to the single glueball states, other states with similar masses and compatible quantum numbers might mix with them and distort the result, i.e. the energy determined by the analysis of the correlation matrix may be dominated by a multi-glueball or torelon state with smaller energy than the single-glueball state to be measured.

In principle, there are several means of determining the nature of a state that has been measured. Firstly, the simulation may be repeated on lattices of different physical size, keeping the lattice spacing fixed. As multi-glueball and torelon states show a finite-volume scaling behaviour very different from single glueballs, such states stand out and may be dropped from further analysis. Secondly, one may measure additional operators that couple strongly to torelon or multi-glueball states. Including or excluding these operators in the variational method and studying the coefficients obtained from the variational method, the mixing strength is determined and states which do not mix considerably with any of the additional operators may be safely considered to be single-glueball states.

Finally, using the mass estimates for the low-lying glueballs, one may determine the approximate locations of the lowest-lying multi-glueball states. Also, the minimal energy of mixing torelons may be estimated using the string formula, eq. (23).

The first two of the methods mentioned above require additional work and computer time and go beyond the scope of this work. The last method, however, can be done rather easily. Let us first calculate the energy of the lowest-lying torelon states that may interfere with our measurements. Single torelons (see Section 3.2) transform non-trivially under Z_3 symmetry operations; our operators, closed Wilson loops, however, are invariant under these transformations. This means that they cannot create single torelon states, however the creation of two torelons of opposite center charge is possible. If we assume that they do not interact considerably and if our lattice extension is rather large then we can use the simple formula $E_{2T} \approx 2\sigma L$ to estimate the energy of a torelon pair with momentum zero, where σ is the string tension (measured by the static $q\bar{q}$ potential, see Section 3.3.1) and L is the spatial extent of the lattice. Table 14 lists the minimum energies of torelon pairs to be expected on our lattices.

Note, that a state composed of two opposite center charge torelons and with total zero momentum is symmetric under charge conjugation. The operators for $C = -$ states therefore do not create such torelon pairs.

Channel	J	$\beta = 3.15$	$\beta = 3.30$	$\beta = 3.50$
A_1^{++}	0	2.58(9)	3.55(13)	3.65(15)
A_1^{++*}	0	5.47(53)	6.83(37)	6.49(148)
E^{++}	2	5.63(23)	5.93(15)	6.08(28)
E^{++*}	2	7.95(73)	8.76(48)	10.66(59)
T_2^{++}	2	5.67(25)	5.82(13)	6.13(16)
T_2^{++*}	2		7.97(69)	10.16(30)
A_2^{++}	3	6.71(73)	9.11(64)	10.92(48)
A_2^{++*}				14.12(130)
T_1^{++}	3	7.54(68)	9.00(44)	11.21(33)
T_1^{++*}		8.69(91)		
A_1^{-+}	0	6.36(59)	6.13(28)	6.79(27)
A_1^{-+*}				10.27(110)
E^{-+}	2	7.41(48)	8.23(28)	8.48(29)
E^{-+*}		8.35(125)		12.66(84)
T_2^{-+}	2	7.41(49)	8.18(21)	8.57(42)
T_2^{-+*}				15.08(67)
T_1^{+-}	1	7.20(39)	7.69(26)	9.12(24)
A_2^{+-}	3			11.02(68)
A_2^{+-*}				15.55(147)
T_2^{+-}		7.75(87)		10.29(118)
T_2^{+-*}				14.98(139)
E^{+-}				12.42(42)
T_1^{--}				10.81(83)
T_2^{--}				10.85(83)
A_2^{--}				12.18(45)
A_1^{--}				15.34(103)

Table 13: Final glueball mass estimates in terms of the hadronic scale r_0 , $m_G r_0$ from the measurements using the perfect $\xi = 2$ action. The continuum spin assignment J is given as well.

β	$r_0 E_{2T}$
3.15	10.60
3.30	8.24
3.50	6.92

Table 14: The minimum energies of momentum zero torelon pairs on the lattices used in the glueball simulations, given in units of r_0^{-1} .

To estimate the lowest energies of multi-glueball states present on our lattices, we follow the method used by Morningstar and Peardon [13], described in great detail in Appendix F of [39]. We assume that the energy of multi-glueball states is approximately given by the sum of the energies of the individual glueballs, i.e. that there is no substantial interaction. It is therefore clear that the lowest-lying multi-glueball states with zero total momentum are the two-glueball states, with energy

$$E_{2G} \approx \sqrt{\vec{p}^2 + m_1^2} + \sqrt{\vec{p}^2 + m_2^2}, \quad (37)$$

where m_1 denotes the rest mass of the first glueball with momentum \vec{p} and m_2 denotes the rest mass of the second glueball with momentum $-\vec{p}$. The masses are taken from our determinations at the respective values of β and the (lattice) momenta are chosen such that the energy E_{2G} of the glueball pair contributing to some representation Γ^{PC} is minimised. Note, that glueball pairs contribute to different representations of the cubic group, not only depending on the representations according to which the single glueballs transform, but also on the single glueball momentum \vec{p} .

The lower bounds of the multi-glueball energy region as well as the lower bound for torelon pairs are indicated in Figures 7–9, together with the determined energies of all the states in the respective representations. It turns out that all of the excited states measured and even some of the lowest states in a given representation could be affected by torelon pairs or multi-glueball states. Of course, it is not at all ruled out that these states are indeed single glueballs, however one has to be very careful with the interpretation and has to keep in mind that these issues require further study.

3.5.6 The Continuum Limit

In order to remove discretisation errors from glueball masses $r_0 m_G$ obtained at finite lattice spacing, we have to perform the continuum limit, i.e. to extrapolate the results to $a_s = 0$. Having obtained results at three values of the coupling β , one of them corresponding to a rather coarse lattice spacing, and having no accurate information (e.g. from perturbation theory) about the behaviour of

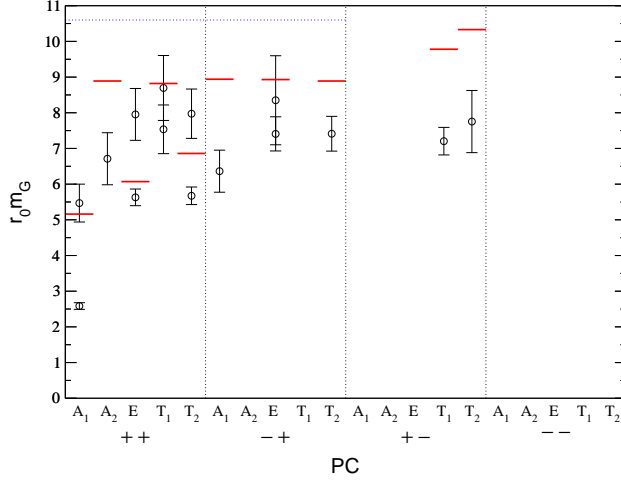


Figure 7: The results of the glueball measurements at $\beta = 3.15$ converted into units of r_0 . The lower bounds of the energies of multi-gluon states (solid lines) or torelon pairs (dotted line) are given as well.

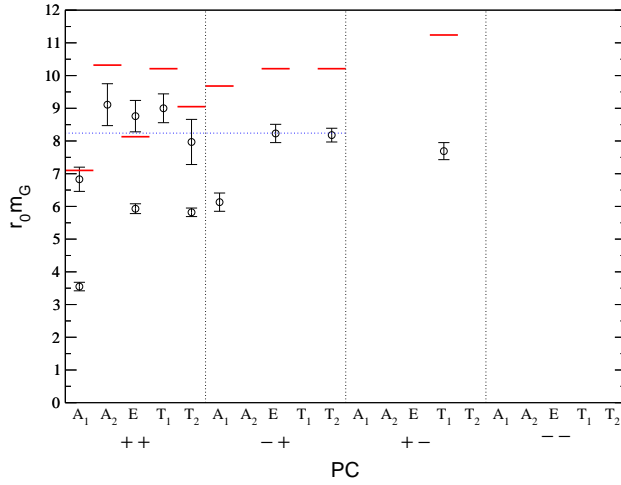


Figure 8: The results of the glueball measurements at $\beta = 3.30$ converted into units of r_0 . The lower bounds of the energies of multi-gluon states (solid lines) or torelon pairs (dotted line) are given as well.

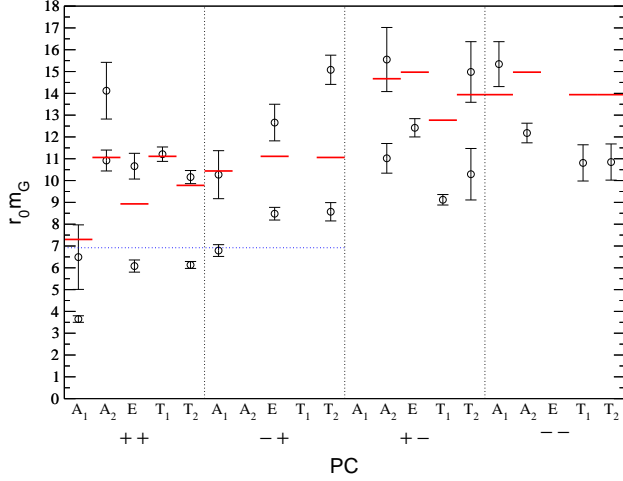


Figure 9: The results of the glueball measurements at $\beta = 3.50$ converted into units of r_0 . The lower bounds of the energies of multi-glueball states (solid lines) or torelon pairs (dotted line) are given as well.

the energies depending on the cut-off (about the form of the curve used in the extrapolation) this is not an easy task and rather ambiguous.

We perform two different kinds of continuum limits. Firstly, we extrapolate the masses in terms of the hadronic scale r_0 , $r_0 m_G = m_G a_t \cdot \xi \cdot r_0 / a_s$, secondly, we extrapolate mass ratios m_{G_1} / m_{G_2} of different glueball representations. Generally, the procedure we resort to is the following: We include all the three energies or mass ratios, obtained at $\beta = 3.15, 3.30, 3.50$, into the fit and use the form

$$r_0 m_G |_{a_s} = r_0 m_G |_{a_s=0} + c_2 \left(\frac{a_s}{r_0} \right)^2, \quad (38)$$

thus including the correction of the smallest power of the (spatial) lattice spacing a_s to be expected to occur. Additionally, we perform fits including only the results from the two finer lattices at $\beta = 3.30, 3.50$ using a constant (if this fits the results reasonably well) or the form stated above. This value of the continuum mass (or mass ratio) is then compared to the result of the fit of all the three data points, which is only accepted if the two results coincide within their errors.

Masses in Terms of r_0

For the extrapolation of masses in terms of the hadronic scale r_0 , this procedure works very well for the representations A_2^{++} , E^{-+} , E^{++} , E^{++*} , T_2^{-+} and T_2^{++} where we may always fit the results from the two finer lattices to a constant which agrees with the result of the extrapolation using eq. (38) on all three data points. For the A_1^{-+} representation, we obtain the best results from fits with a constant to two as well as to three data points.

Much more difficult is the extrapolation for the scalar glueball and its excited state, A_1^{++} and A_1^{++*} . It turns out that the fits have bad values of χ^2 and for the ground state determinations the result obtained performing a fit to a constant mass using the results from the two finer lattices does not correspond to the fit including the third, coarser lattice and a quadratic term in a_s . We decide to keep the (usual) result, including the quadratic term and keep in mind that there may be present some ambiguities which will be discussed later.

The results of the continuum extrapolations for various glueball states are collected in Table 32. In Figures 10 and 11 the fitting curves are shown together with the measured values for the $PC = ++$ and the $PC = -+$ sectors where extrapolations are possible with our data.

Other representations where energies can be determined at several values of β , such as T_1^{+-} , T_1^{++} or T_2^{++*} , do not yield consistent results using the procedure presented above and we decide to abstain from performing continuum extrapolations in terms of $r_0 m_G$ for these states.

Mass Ratios

Extrapolating glueball mass ratios m_{G_1}/m_{G_2} to the continuum has the advantage that uncertainties present in the determination of r_0/a_s and the renormalised anisotropy ξ_R cancel out. Furthermore, we may assume that finite size effects are similar for glueball states measured on the same lattice as opposed to completely different quantities used e.g. to obtain r_0/a_s and ξ_R .

The common way of extrapolating glueball mass ratios to the continuum is using ratios $m_G/m_{0^{++}}$, i.e. ratios to the scalar glueball mass, which is the lightest mass present. Doing this, we observe that the extrapolation is difficult, the value of χ^2 of the fit is rather bad and the errors are large. Furthermore, the resulting continuum mass ratios are not in good agreement to ratios of the continuum masses extrapolated in terms of r_0 . This is not a surprise, because the behaviour of the scalar glueball as a function of the lattice spacing is rather complicated, i.e. there are large cut-off effects that cannot be described too easily. Additionally, the errors of the mass estimates of the scalar glueball are quite large. Due to these reasons, we decide to use the well measured mass of the tensor T_2^{++} representation, which show small errors and seem to scale rather well.

The procedure of the extrapolation is the same as in the case of $r_0 m_G$ described in the previous section; the unambiguous results are listed in Table 33. Again, for the A_1^{-+} states, as well as for the E^{++} , the fit to a constant works

out best. Note, that in this way we can obtain reliable continuum results for the representations T_1^{+-} , T_1^{++} and T_2^{++*} which is not possible performing the extrapolation using masses in terms of r_0 . Furthermore, all the other results listed are in agreement to the ratios of the continuum masses $r_0 m_G$ within one standard deviation.

In the following, we will use the finite lattice spacing results from the simulation on the finest lattice at $\beta = 3.50$ for the energies of states that cannot be extrapolated to the continuum in one of the two ways, e.g. to study degeneracies or to draw a (rather qualitative) picture of the low-lying glueball spectrum. In tables listing continuum results, the values not extrapolated to $a_s = 0$ will be stated in square brackets.

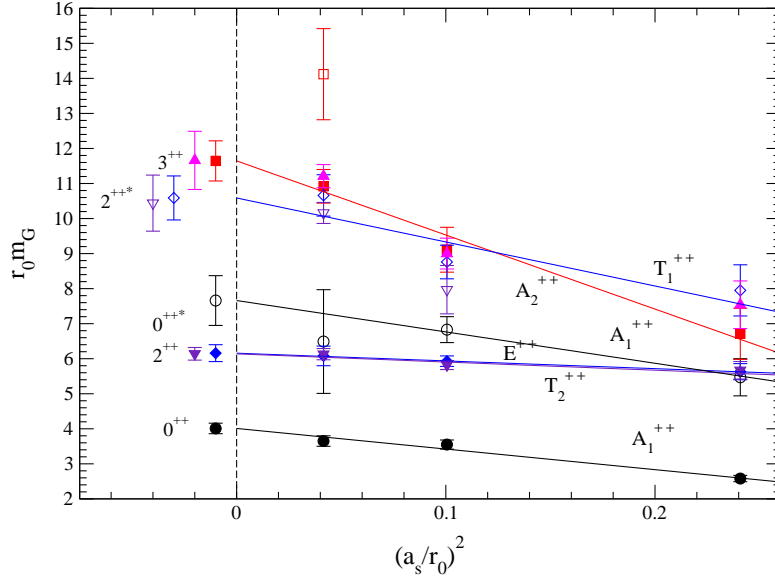


Figure 10: Mass estimates of the $PC = ++$ glueballs in terms of the hadronic scale r_0 against $(a_s/r_0)^2$. The curves are the continuum limit extrapolations of the forms as indicated in the text. *Circles:* A_1^{++} , *boxes:* A_2^{++} , *diamonds:* E^{++} , *upward triangles:* T_1^{++} , *downward triangles:* T_2^{++} ; *solid symbols:* ground states, *open symbols:* first excited states. Note that the continuum results of the representations T_1^{++} and T_2^{++*} have been obtained using a fit of glueball mass ratios.

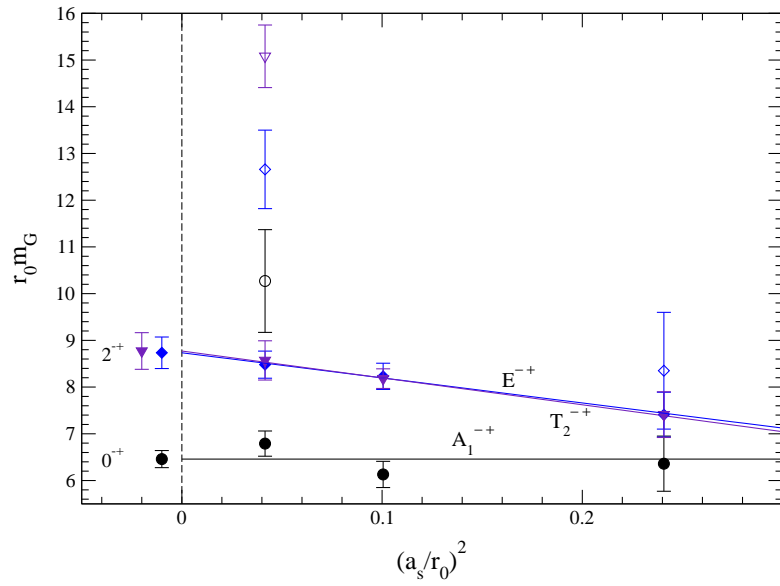


Figure 11: Mass estimates of the $PC = -+$ glueballs in terms of the hadronic scale r_0 against $(a_s/r_0)^2$. The curves are the continuum limit extrapolations of the form $r_0 m_G + c_2(a_s/r_0)^2$. *Circles*: A_1^{-+} , *diamonds*: E^{-+} , *downward triangles*: T_2^{-+} ; *solid symbols*: ground states, *open symbols*: first excited states.

3.5.7 Continuum Spin Identification

Once the extrapolation of the measured glueball energies to the continuum, $a_s = 0$, has been performed, what remains is the assignment of continuum spin J to the different representations of the cubic group Γ . From Table 11 we know from which lattice representations Γ^{PC} a continuum glueball with quantum numbers J^{PC} may obtain contributions, where the assignment of parity P and charge conjugation C is simply one to one. Degeneracies (in the continuum limit) between several representations Γ^{PC} contributing to the same continuum state J^{PC} are a strong indication for the correctness of the assignment of all the lattice states involved to the same continuum J^{PC} glueball. Furthermore, we make the assumption that the mass of the glueballs increases with the spin getting larger.

In the $PC = ++$ sector, we observe a single low-lying state, A_1^{++} , which is thus assigned $J = 0$. The E^{++} and T_2^{++} states are degenerate to a very high precision as it should happen if these representations correspond to the five polarisations of a $J = 2$ glueball. The excited state A_1^{++*} again has no degenerate partner and is assigned to an excited state of the continuum $J = 0$ glueball. The excited states E^{++*} and T_2^{++*} again turn out to be degenerate and so they are assigned to an excitation of the $J = 2$ glueball. The same situation is met with the representations A_2^{++} and T_1^{++} which are thus assigned $J = 3$. Since the first excitation T_2^{++*} is part of the $J = 2$ state, the missing 3 polarisations should come from the second excitation of T_2^{++} which, however, cannot be measured by our simulations.

In the $PC = -+$ sector, the situation of the A_1^{-+} and the E^{-+} and T_2^{-+} is very similar to the one of their partners in the $PC = ++$ sector; these states are thus assigned $J = 0$ and $J = 2$ respectively. The remaining three, excited states have no apparent degeneracies, there is thus no safe assignment of continuum spin to these states. The facts that the excited state A_1^{-+*} is rather light and comes with no degenerate partner, raises the presumption that it is the excited $J = 0^{-+}$ glueball.

In the other two sectors, continuum extrapolations of our measured energies are not possible, except for the representation T_1^{+-} using mass ratios. However, looking at the degenerate representations in the $PC = ++, -+$ sectors, it is noticeable that the degeneracies are apparent even for finite lattice spacing at $\beta = 3.50, 3.30$. Assuming that this behaviour persists for $PC = +-, --$, at least for energies not too high, we may assign continuum spin even to some of the remaining states.

In the $PC = +-$ sector, we notice the lowest-lying T_1^{+-} state having no degenerate partner thence suggesting a $J = 1$ interpretation. Next, there is the A_2^{+-} which is likely to correspond to $J = 3$, which is the smallest possible spin corresponding to this representation.

Finally, in the $PC = --$ sector, there are different possible scenarios. The almost exact degeneracy of T_1^{--} and T_2^{--} suggests them contributing to the $J = 3$ continuum state. The rather heavier state A_2^{--} could still be degenerate with the two latter states (note the high mass and the finite lattice spacing!)

and carry the remaining polarisation. Admittedly, it could as well correspond to an excited $J = 3$ state or even to $J = 6$. The final A_1^{--} state is very heavy and indicates that glueballs with even spin and $PC = --$ have large energies as the representation A_1 contributes solely to even numbered spin states up to $J = 8$.

Let us remark that a new method of improving the overlap of operators to glueballs of a given continuum spin J thus rectifying the continuum spin identification is presented in [64, 65].

The well supported continuum spin assignments presented above are given together with the glueball masses in Tables 13, 32, 33, while the final results on the masses of these states are collected, together with the masses in MeV, in Table 15.

J^{PC}	Γ^{PC}	$m_G r_0$	m_G [MeV]
0^{++}	A_1^{++}	4.01(15)	1580(60)
0^{++*}	A_1^{++*}	7.66(71)	3030(280)
2^{++}	E^{++}, T_2^{++}	6.15(15)	2430(60)
2^{++*}	E^{++*}, T_2^{++*}	10.52(51)	4160(200)
3^{++}	A_2^{++}, T_1^{++}	11.65(49)	4600(190)
0^{-+}	A_1^{-+}	6.46(18)	2550(70)
2^{-+}	E^{-+}, T_2^{-+}	8.75(26)	3460(110)
0^{-+*}	A_1^{-+*}	[10.27(110)]	[4060(430)]
1^{+-}	T_1^{+-}	9.45(71)	3730(280)
3^{+-}	A_2^{+-}	[11.02(68)]	[4350(270)]

Table 15: Final results for the masses of continuum glueballs with quantum numbers J^{PC} , obtained from the lattice representations Γ^{PC} . For the conversion to MeV, $r_0^{-1} \approx 0.5 \text{ fm} \approx 395 \text{ MeV}$ has been used. Quantities in brackets have not been extrapolated to the continuum but denote results from the simulation on the finest lattice at $\beta = 3.50$ (corresponding to $a_s = 0.102 \text{ fm}$).

3.5.8 Discussion

In order to discuss the results obtained from the glueball measurements let us first list the sources of problems that may affect our results. Firstly, there are finite size effects; our finest lattice ($\beta = 3.50$) has got a spatial volume of $(1.22 \text{ fm})^3$ which is rather small compared to other volumes used in glueball measurements. The magnitude of finite-size effects depends largely on the quantity studied, more precisely on the form of the glueball wave functions (above

all their extension). Due to the three volumes employed having such different size, finite-size effects may not only systematically shift the lattice results but they can also make reliable continuum extrapolations much more difficult or even impossible.

Secondly, the mass of the scalar glueball A_1^{++} (above all the ground state) shows very large cut-off effects. These could be due to the presence of a critical end point of a line of phase transitions in the fundamental-adjoint coupling plane. Our parametrisation includes in its rich structure operators transforming in the adjoint representation. If the net coupling of the parametrised action (which we do not control during the construction and the parametrisation) lies in a certain region, the effect of the critical end-point on scalar quantities at certain lattice spacings (sometimes called the “scalar dip”) may even be enhanced compared to other (more standard) discretisations with purely fundamental operators. It is important to note that the true classically perfect action is not expected to be sensitive to this critical point, but it is rather the parametrisation which may incidentally cause the sensitivity close to it.

Furthermore, our analysis shows that states consisting of several glueballs or torelon pairs could mix with most of the higher-lying states occurring in our measurements. This makes the interpretation of the measured states more difficult, additionally, systematic effects (e.g. different mass shifts at different values of β because of the different lattice sizes or due to the presence of operators having larger overlap with unwanted states) may again complicate the continuum extrapolation.

There are several possibilities of improving the situation. Firstly, and most simple, improving the statistics may help. This can be seen e.g. by looking at the results of the simulation on the coarsest lattice at $\beta = 3.15$. Although the lattice is coarser, more energies can be determined than on the finer $\beta = 3.3$ -lattice, mainly due to the larger statistics. Additionally, a lot of problems stated previously could be kept under control if for each value of β , we determine the glueball energies on several lattices of different physical size. A way of improving the measurements is systematically studying the operators employed to create and annihilate single glueball states in order to increase their overlap with the single glueballs to be measured and to decrease their overlap with all the other states. This includes the study of other smearing techniques, such as e.g. Teper fuzzing [66]. Conversely, the introduction of operators coupling most strongly to the unwanted multi-glueball or torelon-pair states allows for the calculation of mixing strengths in order to exclude all the unwanted states from further analysis. Another technically rather easy but computationally expensive way of improving the results is performing simulations on additional values of β . This allows for a more detailed study of the continuum limit, especially in the case of non-perturbatively improved actions, where there is no clearcut information about the way how the continuum is approached. Naturally, one has to take care not to go too deep into the strong coupling region as there is not much information about the continuum.

There is one error which is not cured by the measures recommended in the previous paragraph, namely the effects on the scalar states, coming from the

“scalar dip”. Morningstar and Peardon improve the situation by adding a two-plaquette adjoint term with a negative coefficient which results in an approach to the continuum on a trajectory always far away from the dangerous “dip” region [14]. In principle, the classically perfect action could be treated the same way: extract all the operators with adjoint contributions present in the parametrisation, determine their sign and add another (non-linear) constraint to the fit, namely that the action of all these operators together corresponds to an adjoint operator with a certain (negative) coupling. Because of the large freedom in the fit, the inclusion of this single criterion should not impair the quality of the parametrisation considerably.

Collab.	$r_0 m_{0^{++}}$	$r_0 m_{2^{++}}$
UKQCD [67]	4.05(16)	5.84(18)
Teper [68]	4.35(11)	6.18(21)
GF11 [69]	4.33(10)	6.04(18)
M&P [13]	4.21(15)	5.85(8)
Liu [15]	4.23(22)	5.85(23)
FP action	4.12(21)	[5.96(24)]
AICP	4.01(15)	6.15(15)

Table 16: Comparison of the lowest-lying glueball masses in units of r_0 . Values in brackets denote masses obtained at a lattice spacing $a = 0.10$ fm and are not extrapolated to the continuum.

Collab.	$r_0 m_{0^{-+}}$	$r_0 m_{0^{++*}}$	$r_0 m_{2^{-+}}$	$r_0 m_{1^{+-}}$
Teper [68]	5.94(68)	7.86(50)	8.42(78)	7.84(62)
M&P [13]	6.33(13)	6.50(51)	7.55(11)	7.18(11)
FP action	[6.74(42)]		[8.00(35)]	[7.93(78)]
AICP	6.46(18)	7.66(71)	8.75(26)	9.45(71)

Table 17: Comparison of glueball masses in units of r_0 . Values in brackets denote masses obtained at a lattice spacing $a = 0.10$ fm and are not extrapolated to the continuum.

Table 16 and 17 compares our continuum glueball masses obtained with the anisotropic classically perfect action (AICP) to the results of the isotropic FP action as well as to results obtained by other collaborations. There is reasonable agreement between the different determinations of the 0^{++} , 2^{++} , 0^{++*} , 0^{-+} , 2^{-+} glueball masses. The situation for the 1^{+-} state is different, however. This is the heaviest state that occurs in our analysis and correspondingly difficult to

determine on the lattices used, having a rather small anisotropy $\xi = 2$. Thinking of all the possible sources of errors stated above, which are (partly) also present in the analyses of the other groups, we tend to explain this discrepancy with underestimated (or disregarded) systematic errors as discussed previously. In particular, by looking at the finite lattice spacing results for T_1^{+-} in Table (13), we observe that the masses determined on the coarser (and larger) lattices at $\beta = 3.15, 3.30$ coincide with the (continuum) results obtained by other groups and do not even show a significant discrepancy, despite the considerable difference between the lattice spacings. The mass determined on the fine (and small) lattice at $\beta = 3.50$ however, is much higher. This tendency is even amplified by the continuum extrapolation. We suspect that this state exhibits strong finite-size effects pushing up its mass in small volumes.

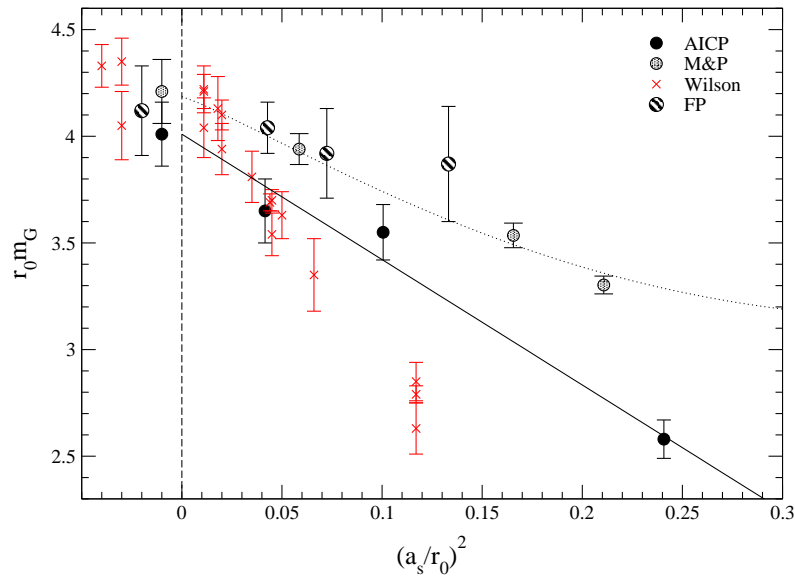


Figure 12: Lattice results and continuum extrapolation of the scalar (0^{++}) glueball mass for the anisotropic classically perfect action, together with results obtained with different other actions. The solid and dotted lines are the continuum extrapolations of the AICP and M&P data, respectively. The different continuum values for the Wilson action stem from different groups.

Figures 12 and 13 compare our measurements of the A_1^{++} , E^{++} and T_2^{++} states to measurements obtained by other groups, using different actions, as well as to the isotropic FP action results. Concerning the scalar glueball, the

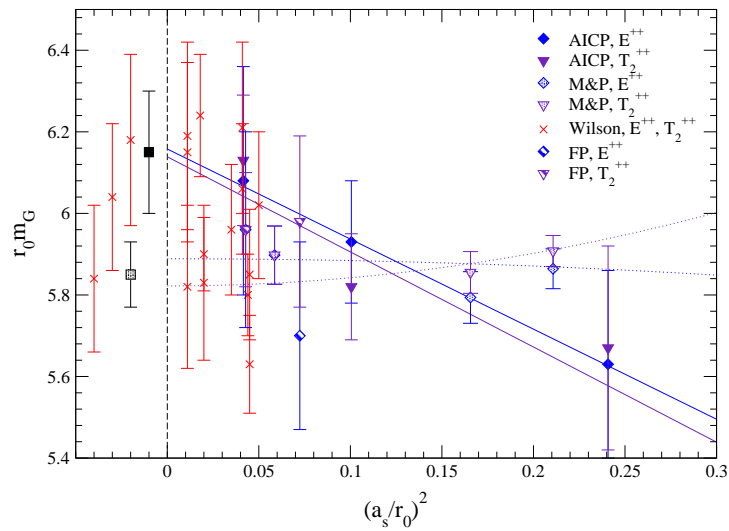


Figure 13: Lattice results and continuum extrapolation of the tensor (2^{++}) glueball mass for the anisotropic classically perfect action, together with results obtained from simulations employing different other actions. The continuum extrapolations of the E^{++} and T_2^{++} representations are averaged in order to get the mass of the single continuum glueball. The solid and dotted lines are the continuum extrapolations of the AICP and M&P data, respectively. The different continuum values for the Wilson action stem from different groups.

artifacts of the isotropic FP action at moderate lattice spacings corresponding to $(a_s/r_0)^2 \lesssim 0.15$ ($a_s \lesssim 0.19$ fm) seem to be rather smaller than the ones of the tadpole and tree-level improved action (M&P) and certainly much smaller than the artifacts of the Wilson action. For the AICP action, however, the situation is less clear. The mass obtained on the coarsest lattice at $\beta = 3.15$ (corresponding to $a_s \approx 0.24$ fm) exhibits large cut-off effects of about 35% (compared to about 20% for the M&P action), probably due to the scalar dip. Concerning the tensor glueball, the picture is not clear, mainly due to the considerable statistical errors of the measurements, except for the ones obtained using the tadpole and tree-level improved anisotropic action.

4 Repeating the Spatial Blocking Step

As noted in section 2, the spatial blocking step used to obtain a classically perfect $\xi = 2$ action may be repeated straightforwardly in order to generate actions with higher anisotropies. Using another spatial scale 2 blocking step we create a classically perfect $\xi = 4$ gauge action and parametrise it in the same way as the $\xi = 2$ action. Furthermore, we measure the renormalised anisotropy and show that it is indeed feasible to construct actions suitable for MC simulations of heavy states such as glueballs. The classically perfect $\xi = 4$ action is not yet examined thoroughly, however the parametrisation is ready (see Appendix A.5) and the analyses of the $\xi = 2$ action (see section 3) may be repeated for $\xi = 4$.

4.1 Construction

Each application of the spatial blocking step (slightly) renormalises the anisotropy of the action; the renormalised anisotropies of the final actions thus have to be measured in the end. However, this is necessary anyhow if one is interested in comparing most results (other than e.g. mass ratios, where the renormalisation of the anisotropy cancels out) to other collaborations or to the experiment.

In order to be able to repeat the spatial blocking step getting from $\xi = 2$ to $\xi = 4$ we construct a $\xi = 2$ action which is valid on minimised $\xi = 4$ configurations including into the fit configurations at different values of β over a large range. The $\xi = 2$ action presented in section 3 is not suitable for this task as it is dedicated to be used solely on largely fluctuating configurations around $\beta = 3.0$. The construction and the parameters of a suitable intermediate $\xi = 2$ action are described in Appendix A.4.

Once the fine action to be used on the r.h.s. of the renormalisation group equation, eq. (1), is ready, we may proceed along the same lines as for the $\xi = 2$ action. We perform the non-linear fit on 2 $\xi_{\text{ad-hoc}} = 6$ configurations each at $\beta_{\text{ad-hoc}} = 4.0, 3.5, 3.0, 2.5, 2.0$. It turns out that in order to obtain parametrisations that are free of dangerous “traps” in the u - w plane (see Section 3.1) we have to include the condition $\mathcal{A}(u, w) > 0$ at ten points (u, w) into the non-linear fit. After studying the values of χ^2 as well as the linear behaviour

of the parametrisations we decide to use a set with $\max(k+l)_{\text{sp}} = 3$ and $\max(k+l)_{\text{tm}} = 2$. The parameters are given in Appendix A.5.

4.2 The Renormalised Anisotropy

To check whether the construction of the classically perfect $\xi = 4$ action works well and whether the parametrisation reproduces the input anisotropy, we measure the renormalised anisotropy at one value of $\beta = 3.0$, using the torelon dispersion relation, following the method described in Section 3.2. The simulation parameters are collected in Table 18.

β	$S^2 \times L \times T$	# sweeps / measurements
3.0	$8^2 \times 4 \times 32$	54000 / 10800

Table 18: Run parameters for the torelon measurements using the $\xi = 4$ perfect action. The lattice extension in torelon direction L , the extension in the two transversal spatial directions S as well as the temporal extension L are given.

Due to the (expected) coarser spatial lattice spacing we do not need as many smearing steps as for the $\xi = 2$ action and thus perform our measurements on smearing levels $\mathcal{S}_n, n = 2, 4, 6, 8, 10$ keeping $\lambda_s = 0.1$ fixed.

Figure 14 displays the dispersion relation so obtained, while Table 34 collects the measured energies $E(p^2)$ determined using variational methods (see Appendix B of [28]), together with the number of operators used in the variational method, the fit ranges and the values of χ^2 per degree of freedom, χ^2/N_{DF} . The renormalised anisotropy as well as the torelon mass are determined in exactly the same way as for the $\xi = 2$ action. The results are listed in Table 19. Furthermore, we may again evaluate an estimate of the lattice scale using the string picture relation, eq. (30), yielding $\sqrt{\sigma}a_s = 0.532(16)$, and thus $r_0/a_s = 2.241(86)$ which corresponds to $a_s = 0.22$ fm, $a_t = 0.060$ fm. Having a torelon of length $La_s \approx 0.89$ fm the error of the scale estimate is expected to be about 5-10% (see Table 5).

β	fit range	ξ_R	$m_{\text{T}}a_t$	χ^2/N_{DF}
3.0	1..5	3.71(8)	0.235(13)	0.82

Table 19: Results of the torelon simulations using the $\xi = 4$ perfect action. The fit range in p^2 is given in units of $(2\pi/S)^2$.

Concerning the repeated application of the spatial blocking method presented in this work to yield classically perfect gauge actions for higher anisotropies, we may conclude that the construction including the blocking as well as the parametrisation works in exactly the same way as the construction of the $\xi = 2$ action. The resulting action shows a renormalisation of the anisotropy of about

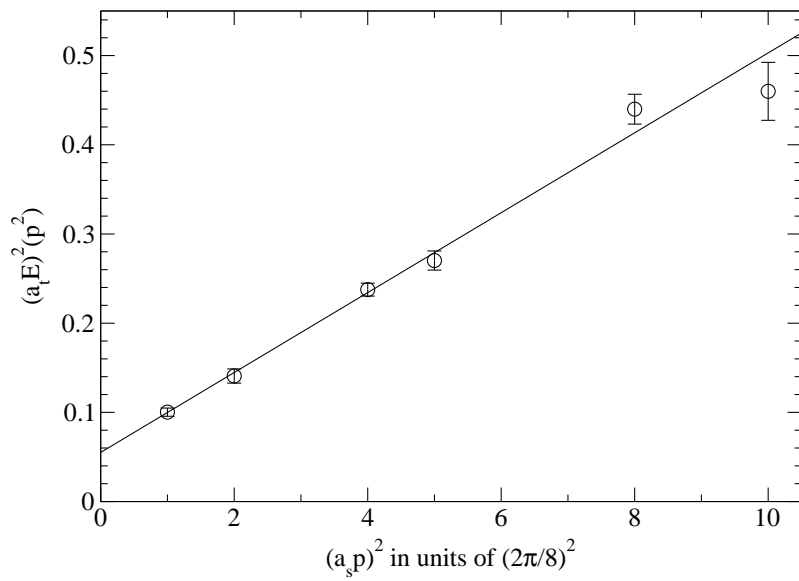


Figure 14: Torelon dispersion relation for $\beta = 3.0$. The straight line is the correlated fit to $E^2(p) = m_T^2 + p^2$ in the range $p^2 = 1..5$.

7% at the value of $\beta = 3.00$ (corresponding roughly to $a_s \simeq 0.2$ fm). Calculations of physical observables such as the static quark-antiquark potential or glueball masses using the $\xi = 4$ classically perfect action are presently absent.

5 Conclusions

In this work, we have presented the construction and parametrisation of a classically perfect anisotropic SU(3) gauge action based on the Fixed Point Action technique. The recently parametrised isotropic FP action and its parametrisation ansatz using mixed polynomials of plaquettes built from single gauge links as well as from smeared links have been the starting point. Performing one and two purely spatial blocking (RG) steps, respectively, starting from the isotropic action, and adapting the parametrisation appropriately, we have obtained parametrised classically perfect actions with anisotropies $\xi = 2$ and 4. The $\xi = 2$ action has been tested extensively in measurements of the torelon dispersion relation, of the static quark-antiquark potential, of the deconfining phase transition as well as of the low-lying glueball spectrum of pure gauge theory.

The results of the torelon measurements show that the renormalisation of the anisotropy (due to quantum corrections and parametrisation artifacts) is small (below 10% for $\xi = 2$ and 4). The rotational invariance of the action has been examined by measuring the static quark-antiquark potential, including separations corresponding to a large set of lattice vectors, again with reassuring results. The glueball measurements, including some rather heavy states, confirm that the use of anisotropic lattices facilitates spectroscopy when heavy states are present. Compared to the isotropic simulations, with the same amount of computational work it is possible to resolve states with considerably larger energy, allowing continuum extrapolations from larger ranges of the lattice spacing. The mass of the scalar glueball with quantum numbers $J^{PC} = 0^{++}$ is measured to be comparable (1580(60) MeV) to masses obtained by other groups (around 1670 MeV); however it shows large cut-off effects when measured on a lattice with spatial lattice spacing $a_s \approx 0.25$ fm. This could be caused by a large sensitivity of the action to a critical point in the fundamental-adjoint coupling plane, due to adjoint terms in the action. Additionally, one has to be aware of the manifold sources of possible errors in measurements of the glueball spectrum. Having at hand the statistics reached so far, no ultimate statement about the goodness of the parametrised classically perfect actions can be made yet.

During our studies of both isotropic and anisotropic classically perfect actions, we have noticed that the examination of scaling properties of lattice gauge actions is a very delicate problem: Quantities which can be reliably measured and which are not very sensitive to systematic factors (like the volume, other states mixing with the observed ones or the method used for extracting the mass etc.), e.g. the critical temperature or the hadronic scale r_0 (for moderate lattice spacings) generally exhibit rather small cut-off effects and thus demand

very large statistics, if the differences between the actions should be explicitly identified. On the other hand, some glueball states show large cut-off effects which makes them interesting objects to study scaling violations. As pointed out in this work, however, there are a lot of systematic factors making the extraction of lattice artifacts difficult. The task of comparing different actions is even more difficult if the measurements and analyses are performed independently by different groups as this introduces additional systematic discrepancies and ambiguities.

Let us therefore conclude that despite the rich parametrisation which allows for all the beautiful properties of classically perfect actions like scale invariance of instanton solutions or rotational invariance, there is no conclusive evidence of the parametrised classically perfect actions (isotropic as well as anisotropic) behaving significantly better than other improved actions (such as the tadpole and tree-level improved anisotropic gauge action) — however, there is also no evidence for the converse. Certainly, one has to consider the large overhead of the parametrisation as compared to other actions if one is about to plan pure gauge simulations.

For the future, very accurate scaling tests comparing the classically perfect actions to other improved gauge actions are desirable. On one hand, these can include large statistics measurements of the critical temperature and the hadronic scale, on the other hand, one might perform extensive simulations of the glueball spectrum, including all the limits to be taken and systematically excluding all known sources of errors.

With respect to the glueball measurements another promising plan would be to gain control about the adjoint operators present in the parametrisation of the classically perfect actions in order to circumvent the critical point in the adjoint coupling plane such that the influence of the scalar dip is minimised, similarly to what has been done for the tree-level and tadpole improved actions by Morningstar and Peardon [14].

Acknowledgements: We would like to thank Ferenc Niedermayer and Peter Hasenfratz for valuable discussions. Further thanks go to Simon Hauswirth, Thomas Jörg and Michael Marti for computer support. U.W. acknowledges support by a PPARC special grant.

A Action Parameters

In this Appendix we collect the parameters of the FP and the classically perfect actions that have been used or constructed throughout this work. The isotropic FP action for coarse configurations has been presented already in [28]. The isotropic action in Section A.1 is an intermediate parametrisation valid on configurations typical for MC simulations that are minimised once, parametrised during the cascade process for the isotropic action. It is used in the spatial blocking (see Section 3.1) to minimise the coarse $\xi = 2$ configurations, constructed using the ad-hoc anisotropic action presented in Section A.2. The resulting $\xi = 2$ perfect action for coarse configurations is presented in Section A.3.

To repeat the blocking step, we need a $\xi = 2$ action which is valid for $\xi = 4$ configurations minimised once in a purely spatial blocking step. This action is described in Section A.4. The resulting $\xi = 4$ action, finally, is presented in Section A.5.

A.1 The Intermediate Isotropic Action

The intermediate isotropic action has been parametrised during the construction of the isotropic FP action. It is supposed to be valid on configurations that are obtained by minimising configurations typical for MC simulations. It fulfills the $O(a^2)$ Symanzik conditions (see [40, 28]) and uses polynomials in the fluctuation parameter $x_\mu(n)$, thence it smoothly approaches the continuum limit and is expected to interpolate between the rather coarse configurations mentioned above and the smooth limit. It is not intended to be used in MC simulations, since its linear behaviour (see Section 3.1) is not checked.

This action has been used for the (spatial) minimisation of coarse $\xi = 2$ configurations, i.e. to describe the isotropic configurations on the r.h.s. of eq. (1).

The non-linear parameters describing polynomials of order 3 are (cf. formula (8), (7) and (11), (12)):

$$\begin{aligned} \eta^{(0)} &= 0.082, & \eta^{(1)} &= 0.292353, & \eta^{(2)} &= 0.115237, & \eta^{(3)} &= 0.011456, \\ c_1^{(0)} &= 0.282, & c_1^{(1)} &= -0.302295, & c_1^{(2)} &= -0.302079, & c_1^{(3)} &= -0.052309, \\ c_2^{(0)} &= 0.054, & c_2^{(1)} &= 0.298882, & c_2^{(2)} &= -0.081365, & c_2^{(3)} &= -0.023762, \\ c_3^{(0)} &= -0.201671, & c_3^{(1)} &= 0.022406, & c_3^{(2)} &= 0.004090, & c_3^{(3)} &= 0.014886, \\ c_4^{(0)} &= -0.008977, & c_4^{(1)} &= 0.245363, & c_4^{(2)} &= 0.140016, & c_4^{(3)} &= 0.028783. \end{aligned}$$

The linear parameters are collected in Table 20.

p_{kl}	$l = 0$	$l = 1$	$l = 2$	$l = 3$	$l = 4$
$k = 0$		0.629227	-0.556304	0.186662	-0.010110
$k = 1$	-0.368095	0.852428	-0.199034	0.031614	
$k = 2$	0.389292	-0.207378	-0.010898		
$k = 3$	-0.054912	0.039059			
$k = 4$	-0.000424				

Table 20: The linear parameters p_{kl} of the parametrised intermediate isotropic FP action.

A.2 “Ad-hoc” Anisotropic Actions

In the spatial blocking procedure described in section 2 one needs coarse anisotropic ($\xi = 2, 4, 6, \dots$) gauge configurations which are spatially minimised leading to $\xi' = \xi/2$ configurations. As the goal of this step is to obtain a perfect anisotropic

action with anisotropy ξ these coarse anisotropic configurations have to be produced using some other action that is already present. This requirement might seem to endanger the whole ansatz, however it is not crucial how the coarse configurations exactly look like as the perfectness of the resulting coarse action comes from the perfect action on the fine configuration as well as from the exactness of the RG transformation. Still, we try to create coarse configurations that might look similar to future ensembles produced using the perfect anisotropic action on the coarse level and whose minimised configurations appear to have an anisotropy approximately $\xi' = \xi/2$.

In order to achieve this, we modify the isotropic FP action by adding a term $(\xi^2 - 1)p_{10}^{st}$ (where p_{10}^{st} denotes the simple temporal plaquette). This modification turns the isotropic Wilson action into the Wilson action with bare anisotropy ξ and is expected to work approximately also for our FP action. The main argument of using this coarse action and not e.g. the anisotropic Wilson action is that due to the spatial lattice spacing a_s being larger than the temporal spacing a_t , the $O(a_s^2)$ artifacts are also expected to be larger than the $O(a_t^2)$ effects. The modification described above should (approximately) preserve the FP properties corresponding to a_s and is thus expected to be considerably better than the naive anisotropic Wilson action.

Using this ad-hoc modification of the isotropic FP action (“ad-hoc” action) in MC simulations shows (as expected) that (at least for small anisotropies $\xi \lesssim 5$) its properties on the glueball spectrum are not comparable with the ones of the isotropic FP action, however the generated ensembles resemble to the ones generated with true perfect anisotropic actions much more than ensembles generated with the Wilson action.

The anisotropies $\xi_{\text{ad-hoc}}$ that have to be used to generate coarse anisotropic configurations turning into minimised configurations with anisotropy ξ' are $\xi_{\text{ad-hoc}} \approx 3.2$ for $\xi' = 1$ and $\xi_{\text{ad-hoc}} \approx 6$ for $\xi' = 2$. However, this value of $\xi_{\text{ad-hoc}}$ varies considerably with β — but as stated at the beginning of this section, the exact form of the coarse configurations is not essential.

A.3 The $\xi = 2$ Perfect Action

The $\xi = 2$ perfect action uses the parametrisation described in Section 2.3. The number of non-zero asymmetry values $\eta_i^{(0)}$ is 4, the parameters $c_i^{(0)}$ ($i = 1, \dots, 3$) are splitted into 3 parameters depending on the contribution to the smeared plaquette. The linear parameters p_{kl} are non-zero for $0 < k + l \leq 4$ for spatial plaquettes and $0 < k + l \leq 3$ for temporal plaquettes.

The non-linear parameters (constants in x_μ) have the values

$$\begin{aligned} \eta_1 &= -0.866007, & \eta_2 &= -0.884110, & \eta_3 &= 2.212499, & \eta_4 &= 1.141177; \\ c_{11} &= 0.399669, & c_{12} &= 0.519037, & c_{13} &= -0.071334, \\ c_{21} &= -0.076357, & c_{22} &= -0.031051, & c_{23} &= -0.282800, \\ c_{31} &= 0.032396, & c_{32} &= -0.015844, & c_{33} &= -0.046302. \end{aligned}$$

The linear parameters are collected in Table 21

p_{kl}^{ss}	$l = 0$	$l = 1$	$l = 2$	$l = 3$	$l = 4$
$k = 0$		0.433417	0.098921	-0.116251	0.023295
$k = 1$	0.217599	-0.272668	0.248188	-0.045278	
$k = 2$	0.316145	-0.180982	0.028817		
$k = 3$	-0.039521	0.003858			
$k = 4$	0.005443				
p_{kl}^{st}	$l = 0$	$l = 1$	$l = 2$	$l = 3$	
$k = 0$		-0.190195	0.554426	-0.121766	
$k = 1$	1.521212	-0.328305	0.086655		
$k = 2$	0.011178	0.020932			
$k = 3$	0.022856				

Table 21: The linear parameters of the $\xi = 2$ parametrised classically perfect action.

A.4 The $\xi = 2$ Intermediate Action

In order to be able to repeat the spatial blocking step constructing a $\xi \approx 4$ action based on the $\xi = 2$ perfect action we need a parametrisation of the $\xi = 2$ action which is valid on ($\xi \approx 2$) configurations that are obtained by spatially minimising coarse $\xi = 4$ configurations once. To construct such an action, we perform a non-linear fit to the derivatives of 5 sets of two configurations each at $\beta_{\text{ad-hoc}} = 6, 10, 20, 50, 100$. The non-linear parameters are chosen to be linear in the fluctuation parameter $x_\mu(n)$. Having four different parameters η and splitting up c_i into three parameters (as it is done for all anisotropic parametrisations), this makes 20 non-linear parameters to be fitted which is quite at the edge of what is still possible on our computers and that is why we restrict the total number of configurations to 10. Rough checks performed on a larger number of configurations, with an even larger number of parameters show however, that the resulting non-linear parameters are stable and describe the data accurately.

The derivatives and action values of 5 sets of 10 configurations each are included in the linear fit (where the relative weight of the action values is chosen to be $1.9 \cdot 10^{-2}$ for the configurations at $\beta_{\text{ad-hoc}} = 50, 100$ and $7.6 \cdot 10^{-4}$ at $\beta = 6, 10, 20$). A linear set where the parameters p_{kl} are non-zero for $0 < k + l \leq 3$ for spatial plaquettes and $0 < k + l \leq 4$ for temporal plaquettes describes the full action very well concerning this data. Again, this parametrisation is not intended to be used in MC simulations, thus the linear behaviour of the action is not checked.

The non-linear parameters (up to first order in x_μ) have the values

$$\begin{aligned}
\eta_1^{(0)} &= -1.861267, & \eta_1^{(1)} &= -0.327466, & \eta_2^{(0)} &= -1.075610, & \eta_2^{(1)} &= -0.550398, \\
\eta_3^{(0)} &= 2.750293, & \eta_3^{(1)} &= 0.089874, & \eta_4^{(0)} &= 1.107017, & \eta_4^{(1)} &= 0.265817; \\
c_{11}^{(0)} &= 0.520960, & c_{11}^{(1)} &= 0.006339, & c_{21}^{(0)} &= -0.075219, & c_{21}^{(1)} &= 0.059506 \\
c_{12}^{(0)} &= 0.266240, & c_{12}^{(1)} &= 0.121035, & c_{22}^{(0)} &= -0.080771, & c_{22}^{(1)} &= -0.021515 \\
c_{13}^{(0)} &= 0.159372, & c_{13}^{(1)} &= 0.039564, & c_{23}^{(0)} &= -0.043901, & c_{23}^{(1)} &= 0.009672
\end{aligned}$$

The linear parameters are collected in Table 22

p_{kl}^{ss}	$l = 0$	$l = 1$	$l = 2$	$l = 3$	
$k = 0$		0.088016	0.002225	-0.000285	
$k = 1$	0.341850	-0.015888	-0.004087		
$k = 2$	-0.053007	0.010121			
$k = 3$	0.010500				
p_{kl}^{st}	$l = 0$	$l = 1$	$l = 2$	$l = 3$	$l = 4$
$k = 0$		0.280043	5.077727	-13.714872	12.739964
$k = 1$	1.343946	-6.934825	27.673937	-32.288928	
$k = 2$	2.069084	-17.392027	28.248910		
$k = 3$	3.691733	-9.584760			
$k = 4$	0.712244				

Table 22: The linear parameters of the intermediate $\xi = 2$ parametrised classically perfect action.

A.5 The $\xi = 4$ Perfect Action

The $\xi = 4$ perfect action uses the parametrisation described in Section 2.3. The number of non-zero asymmetry values $\eta_i^{(0)}$ is 4, the parameters $c_i^{(0)}$ ($i = 1, \dots, 3$) are splitted into 3 parameters depending on the contribution to the smeared plaquette. The linear parameters p_{kl} are non-zero for $0 < k + l \leq 3$ for spatial plaquettes and $0 < k + l \leq 2$ for temporal plaquettes.

The non-linear parameters (constants in x_μ) have the values

$$\begin{aligned}
\eta_1 &= -1.491457, & \eta_2 &= -1.115141, & \eta_3 &= 1.510985, & \eta_4 &= 7.721347; \\
c_{11} &= 2.014408, & c_{12} &= 0.128768, & c_{13} &= 0.162296, \\
c_{21} &= -0.915620, & c_{22} &= 0.134445, & c_{23} &= -0.013383, \\
c_{31} &= 1.166289, & c_{32} &= 0.061278, & c_{33} &= 0.000759,
\end{aligned}$$

The linear parameters are collected in Table 23

p_{kl}^{ss}	$l = 0$	$l = 1$	$l = 2$	$l = 3$
$k = 0$		0.027625	0.000052	0.000000
$k = 1$	0.072131	-0.016852	-0.000054	
$k = 2$	0.036818	0.003558		
$k = 3$	-0.007413			
p_{kl}^{st}	$l = 0$	$l = 1$	$l = 2$	
$k = 0$		0.795779	0.621286	
$k = 1$	2.130563	-0.286602		
$k = 2$	0.076086			

Table 23: The linear parameters of the $\xi = 4$ parametrised classically perfect action.

B Collection of Results

β	p^2	M	fit range	$a_t E(p^2)$	χ^2/N_{DF}
3.0	0	2	1-5	1.368(30)	0.19
	1	3	1-6	1.372(17)	0.49
	2	3	1-6	1.451(17)	0.28
	4	3	1-8	1.570(21)	0.46
	5	3	1-6	1.610(19)	0.34
	8	2	1-3	1.707(29)	0.05
3.15 ^a	0	3	2-5	0.688(16)	0.11
	1	4	1-5	0.806(5)	0.06
	2	4	1-5	0.902(6)	0.59
	4	3	1-5	1.059(8)	2.35
	5	4	1-5	1.151(7)	0.16
	8	4	1-5	1.310(15)	0.71
	9	4	1-5	1.356(23)	1.58
	10	4	1-3	1.470(17)	0.42
	13	3	1-3	1.621(23)	0.01
	18	3	1-3	1.762(47)	0.56
3.15 ^b	1	3	1-5	1.418(23)	0.05
	2	3	1-5	1.541(37)	0.53
	4	3	1-4	1.751(67)	1.20
	5	3	1-5	1.922(104)	1.08

Table 24: Collection of results of the torelon measurements using the $\xi = 2$ perfect action. For each β -value and momentum $p^2 = p_x^2 + p_y^2$ we list the number of operators M kept after the first truncation in the variational method, the plateau region on which the fit of the correlators to the form $Z(p^2) \exp(-tE(p^2))$ is performed (fit range), as well as the extracted energy together with the χ^2 per degree of freedom (χ^2/N_{DF}). (*Continued in Table 25*)

β	p^2	M	fit range	$a_t E(p^2)$	χ^2/N_{DF}
3.3	0	3	1–10	0.318(6)	1.39
	1	3	1–10	0.417(3)	1.20
	2	3	1–5	0.493(3)	0.13
	4	4	1–4	0.633(4)	1.26
	5	5	1–10	0.688(3)	0.84
	8	5	1–8	0.830(5)	1.21
	9	5	1–6	0.877(6)	0.42
	10	5	1–10	0.921(4)	0.77
	13	5	1–10	1.036(6)	0.30
	18	4	1–6	1.205(12)	0.15
3.5 ^a	1	5	3–8	0.305(6)	0.10
	2	5	1–10	0.407(4)	1.65
	4	4	1–10	0.538(4)	0.96
	5	5	1–10	0.586(3)	1.16
	8	5	1–7	0.721(4)	0.09
	9	5	2–6	0.733(10)	0.11
	10	4	1–8	0.795(4)	0.96
	13	5	1–6	0.901(4)	1.26
	18	5	1–6	1.058(9)	1.45
	3.5 ^b	1	4	3–7	0.321(5)
2		5	1–8	0.432(3)	0.81
4		5	1–8	0.586(4)	0.29
5		5	1–7	0.656(3)	1.24
8		5	2–7	0.806(14)	0.36
9		5	1–7	0.859(7)	0.74
10		5	1–8	0.913(4)	0.68
13		5	2–5	1.010(16)	0.32
18		3	1–5	1.215(12)	0.17

Table 25: Collection of results of the torelon measurements using the $\xi = 2$ perfect action. For each β -value and momentum $p^2 = p_x^2 + p_y^2$ we list the number of operators M kept after the first truncation in the variational method, the plateau region on which the fit of the correlators to the form $Z(p^2) \exp(-tE(p^2))$ is performed (fit range), as well as the extracted energy together with the χ^2 per degree of freedom (χ^2/N_{DF}). (*Continuation from Table 24*)

\vec{r}	$ \vec{r} $	M	fit range	$a_t V(\vec{r})$	χ^2/N_{DF}
(1,0,0)	1	3	3–10	0.3006(1)	0.20
(1,1,0)	1.414	3	3–10	0.3814(2)	0.21
(1,1,1)	1.732	3	3–10	0.4250(3)	0.65
(2,0,0)	2	3	6–10	0.4469(6)	0.22
(2,1,0)	2.236	3	4–10	0.4752(4)	0.41
(2,1,1)	2.449	3	4–10	0.4971(5)	0.83
(2,2,0)	2.828	3	4–10	0.5309(7)	0.59
(3,0,0)	3	3	4–10	0.5445(7)	1.71
(2,2,1)	3	3	5–10	0.5456(8)	0.62
(2,2,2)	3.464	3	4–10	0.5852(9)	1.53
(4,0,0)	4	3	4–10	0.6269(1)	0.51
(3,3,0)	4.243	3	5–10	0.6455(16)	0.94
(4,2,0)	4.472	3	5–10	0.6630(14)	0.86
(4,2,2)	4.899	3	5–10	0.6964(18)	0.34
(5,0,0)	5	2	5–10	0.7044(22)	1.24
(3,3,3)	5.196	3	4–10	0.7215(17)	1.31
(4,4,0)	5.657	2	6–10	0.7509(41)	1.23
(4,4,2)	6	3	5–10	0.7783(25)	0.77

Table 26: Collection of results of the off-axis $q\bar{q}$ measurements using the $\xi = 2$ perfect action at $\beta = 3.30$. For each separation vector we list the length of the vector in spatial lattice units, the number of operators M kept after the first truncation in the variational method, the plateau region on which the fit of the correlators to the form $Z(\vec{r}) \exp(-tE(\vec{r}))$ is performed (fit range), as well as the extracted energy together with the χ^2 per degree of freedom (χ^2/N_{DF}).

\vec{r}	$ \vec{r} $	M	fit range	$a_t V(\vec{r})$	χ^2/N_{DF}
(1,0,0)	1	3	2–7	0.5053(3)	0.70
(1,1,0)	1.414	3	3–5	0.7322(7)	0.01
(1,1,1)	1.732	3	3–8	0.8902(14)	0.60
(2,0,0)	2	3	2–8	0.9407(10)	0.89
(2,1,0)	2.236	3	2–8	1.0642(11)	0.36
(2,1,1)	2.449	2	2–5	1.1676(13)	0.27
(2,2,0)	2.828	3	2–6	1.3082(18)	0.17
(3,0,0)	3	3	2–6	1.3392(25)	0.16
(2,2,1)	3	3	2–5	1.3867(20)	0.26
(2,2,2)	3.464	3	2–6	1.5675(55)	0.84
(4,0,0)	4	2	1–5	1.7429(24)	0.14
(4,2,0)	4.472	3	2–6	1.9328(93)	1.47
(4,2,2)	4.899	3	1–4	2.1197(34)	0.15

Table 27: Collection of results of the off-axis $q\bar{q}$ measurements using the $\xi = 2$ perfect action at $\beta = 3.00$. For each separation vector we list the length of the vector in spatial lattice units, the number of operators M kept after the first truncation in the variational method, the plateau region on which the fit of the correlators to the form $Z(\vec{r}) \exp(-tE(\vec{r}))$ is performed (fit range), as well as the extracted energy together with the χ^2 per degree of freedom (χ^2/N_{DF}).

β	r	M	fit range	$a_t V(r)$	χ^2/N_{DF}
3.15	1	5	3–10	0.3703(2)	0.456
	2	5	3–7	0.6110(4)	0.735
	3	5	3–10	0.8019(8)	1.209
	4	5	3–7	0.9775(16)	1.238
	5	5	4–9	1.129(8)	0.519
3.50	1	5	3–12	0.25910(5)	1.163
	2	5	3–10	0.36490(12)	0.769
	3	5	7–12	0.42168(38)	0.664
	4	5	5–11	0.46587(51)	0.205
	5	5	5–12	0.50388(76)	1.139
	6	5	5–11	0.54051(96)	0.853

Table 28: Collection of results of the on-axis $q\bar{q}$ measurements using the $\xi = 2$ perfect action at $\beta = 3.15, 3.50$. For each separation along the axes we list the number of operators M kept after the first truncation in the variational method, the plateau region on which the fit of the correlators to the form $Z(r)\exp(-tE(r))$ is performed (fit range), as well as the extracted energy together with the χ^2 per degree of freedom (χ^2/N_{DF}).

Channel	N	t_0/t_1	M	fit range	χ^2/N_{DF}	energies
A_1^{++}	87	1/2	12	1 – 4	0.69	0.645(10)
A_1^{++*}	59	1/2	10	1 – 3	1.23	1.365(104)
E^{++}	47	1/2	7	1 – 3	0.10	1.405(29)
E^{++*}	47	1/2	5	1 – 3	0.17	1.985(140)
T_2^{++}	47	1/2	10	1 – 4	0.10	1.416(32)
T_2^{++*}	22	1/2	6	1 – 3	1.20	1.990(131)
A_2^{++}	21	1/2	2	1 – 3	0.03	1.675(147)
T_1^{++}	36	1/2	4	1 – 3	0.34	1.881(131)
T_1^{++*}	36	1/2	6	1 – 3	0.31	2.170(182)
A_1^{-+}	25	1/2	3	1 – 3	0.001	1.588(114)
E^{-+}	25	1/2	2	1 – 3	0.01	1.849(81)
E^{-+*}	25	1/2	2	1 – 3	2.19	2.084(268)
T_2^{-+}	64	1/2	4	1 – 3	0.02	1.850(83)
T_1^{+-}	61	1/2	4	1 – 3	0.24	1.798(59)
T_2^{+-}	18	1/2	4	1 – 3	0.41	1.935(177)

Table 29: Results from fits to the $\xi = 2$, $\beta = 3.15$ glueball correlators on the $8^3 \times 16$ lattice in units of the temporal lattice spacing a_t : t_0/t_1 are used in the generalised eigenvalue problem, N is the number of initial operators measured and M denotes the number of operators kept after the truncation in $C(t_0)$.

Channel	t_0/t_1	M	fit range	χ^2/N_{DF}	energies
A_1^{++}	1/2	9	2 – 7	0.90	0.590(17)
A_1^{++*}	1/2	11	1 – 3	1.57	1.133(53)
E^{++}	1/2	11	1 – 5	0.97	0.983(17)
E^{++*}	1/2	8	1 – 3	0.90	1.453(68)
T_2^{++}	1/2	12	1 – 4	1.09	0.965(15)
T_2^{++*}	1/2	10	1 – 4	1.68	1.386(51)
A_2^{++}	1/2	4	1 – 3	0.01	1.511(94)
T_1^{++}	1/2	8	1 – 5	0.84	1.492(62)
A_1^{-+}	1/2	6	1 – 4	4.38	1.017(39)
E^{-+}	1/2	3	1 – 4	0.74	1.365(36)
T_2^{-+}	1/2	4	1 – 5	1.16	1.357(25)
T_1^{+-}	1/2	8	1 – 4	0.95	1.276(33)

Table 30: Results from fits to the $\xi = 2$, $\beta = 3.3$ glueball correlators on the $10^3 \times 20$ lattice in units of the temporal lattice spacing a_t : t_0/t_1 are used in the generalised eigenvalue problem, M denotes the number of operators kept after the truncation in $C(t_0)$.

Channel	N	t_0/t_1	M	fit range	χ^2/N_{DF}	energies
A_1^{++}	91	1/2	24	2 – 7	0.31	0.405(13)
A_1^{++*}	110	0/1	110	4 – 6	0.30	0.720(158)
E^{++}	104	1/2	23	2 – 5	0.16	0.675(25)
E^{++*}	104	1/2	14	1 – 3	0.70	1.183(55)
T_2^{++}	53	1/2	19	2 – 5	0.31	0.681(12)
T_2^{++*}	53	1/2	22	1 – 3	0.69	1.128(23)
A_2^{++}	15	1/2	6	1 – 3	0.05	1.212(42)
A_2^{++*}	15	1/2	6	1 – 3	1.12	1.568(130)
T_1^{++}	23	1/2	11	1 – 4	0.05	1.245(25)
A_1^{-+}	15	1/2	9	1 – 3	0.17	0.754(23)
A_1^{-+*}	15	1/2	9	1 – 3	0.61	1.140(112)
E^{-+}	21	1/2	14	1 – 3	0.27	0.942(24)
E^{-+*}	21	1/2	11	1 – 3	1.20	1.406(80)
T_2^{-+}	75	1/2	9	2 – 5	0.32	0.952(38)
T_2^{-+*}	75	1/2	6	1 – 3	1.70	1.675(59)
T_1^{+-}	53	1/2	14	1 – 3	0.69	1.013(17)
A_2^{+-}	11	1/2	5	1 – 3	0.07	1.224(64)
A_2^{+-*}	11	1/2	5	1 – 3	0.79	1.726(147)
T_2^{+-}	22	1/2	9	2 – 4	0.33	1.142(121)
T_2^{+-*}	12	1/2	9	1 – 3	1.78	1.663(139)
E^{+-}	50	0/1	50	1 – 3	1.01	1.379(34)
T_1^{--}	80	0/1	80	2 – 4	0.57	1.200(67)
T_2^{--}	80	0/1	80	2 – 5	0.20	1.205(81)
A_2^{--}	35	0/1	35	1 – 3	0.16	1.352(37)
A_1^{--}	30	0/1	30	1 – 4	0.14	1.703(99)

Table 31: Results from fits to the $\xi = 2$, $\beta = 3.5$ glueball correlators on the $12^3 \times 24$ lattice in units of the temporal lattice spacing a_t : t_0/t_1 are used in the generalised eigenvalue problem, N is the number of initial operators measured and M denotes the number of operators kept after the truncation in $C(t_0)$.

Channel	J	terms in the fit	χ^2/N_{DF}	$r_0 m_G$
A_1^{++}	0	c, c_2	2.72	4.01(15)
A_1^{++*}	0	c, c_2	1.43	7.66(71)
E^{++}	2	c, c_2	1.06	6.16(24)
E^{++*}	2	c, c_2	3.85	10.59(63)
T_2^{++}	2	c, c_2	1.98	6.14(18)
A_2^{++}	3	c, c_2	1.65	11.65(57)
A_1^{-+}	0	c	2.50	6.46(18)
E^{-+}	2	c, c_2	1.06	8.73(34)
T_2^{-+}	2	c, c_2	1.07	8.77(39)

Table 32: Results of the continuum extrapolations of selected glueball representations in terms of the hadronic scale r_0 . The continuum spin assignment J , the terms in the fit, constant (c) or $(a_s/r_0)^2$ (c_2), and the goodness of the fit, χ^2/N_{DF} , are also given.

Γ^{PC}	J	terms in the fit	χ^2/N_{DF}	$m_{\Gamma^{PC}}/m_{T_2^{++}}$	$r_0 m_G$
E^{++}	2	c	1.20	1.01(2)	6.20(30)
E^{++*}	2	c, c_2	2.20	1.74(12)	10.68(105)
T_2^{++*}	2	c, c_2	3.01	1.70(8)	10.44(80)
A_2^{++}	3	c, c_2	1.11	1.90(11)	11.66(102)
T_1^{++}	3	c, c_2	2.60	1.90(8)	11.66(83)
A_1^{-+}	0	c	1.39	1.09(4)	6.69(44)
T_2^{-+}	2	c, c_2	1.23	1.45(8)	8.90(75)
T_1^{+-}	1	c, c_2	2.29	1.54(7)	9.45(71)

Table 33: Results of the continuum extrapolations of selected glueball ratios, $m_G/m_{T_2^{++}}$. The continuum spin assignment J , the terms in the fit, constant (c) or $(a_s/r_0)^2$ (c_2), and the goodness of the fit, χ^2/N_{DF} , are also given. The last column lists the masses converted to units of r_0^{-1} using the continuum result for the mass of the tensor glueball T_2^{++} , values in bold face will be used further on.

β	p^2	M	fit range	$a_t E(p^2)$	χ^2/N_{DF}
3.0	1	5	3–10	0.317(5)	1.34
	2	3	4–10	0.375(8)	0.31
	4	3	3–11	0.487(7)	0.65
	5	5	4–11	0.520(11)	0.35
	8	5	3–7	0.663(17)	0.09
	9	3	4–11	0.754(37)	0.87
	10	5	4–11	0.678(32)	1.56

Table 34: Collection of results of the torelon measurement at $\beta = 3.0$, using the $\xi = 4$ perfect action. For each momentum $p^2 = p_x^2 + p_y^2$ we list the number of operators M kept after the first truncation in the variational method, the plateau region on which the fit of the correlators to the form $Z(p^2) \exp(-tE(p^2))$ is performed (fit range), as well as the extracted energy together with the χ^2 per degree of freedom (χ^2/N_{DF}).

References

- [1] Lattice hadron physics, F. X. Lee, Nucl. Phys. Proc. Suppl. **94**, 251 (2001), hep-lat/0011060.
- [2] CP-PACS, A. Ali Khan *et al.*, Nucl. Phys. Proc. Suppl. **94**, 325 (2001), hep-lat/0011005.
- [3] P. Chen, (2000), hep-lat/0006019.
- [4] P. Chen, X. Liao and T. Manke, Nucl. Phys. Proc. Suppl. **94**, 342 (2001), hep-lat/0010069.
- [5] R. Lewis and R. M. Woloshyn, Nucl. Phys. Proc. Suppl. **83**, 316 (2000), hep-lat/9909106.
- [6] R. Lewis and R. M. Woloshyn, Phys. Rev. **D62**, 114507 (2000), hep-lat/0003011.
- [7] J. Shigemitsu, Nucl. Phys. Proc. Suppl. **94**, 371 (2001), hep-lat/0010029.
- [8] A. A. Darmohval, V. K. Petrov and G. M. Zinovjev, (1999), hep-lat/9906003.
- [9] G. S. Bali, Nucl. Phys. Proc. Suppl. **83**, 422 (2000), hep-lat/9908021.
- [10] S. Deldar, Nucl. Phys. Proc. Suppl. **83**, 440 (2000), hep-lat/9909077.
- [11] S. Deldar, Phys. Rev. **D62**, 034509 (2000), hep-lat/9911008.
- [12] C. J. Morningstar and M. J. Peardon, Phys. Rev. **D56**, 4043 (1997), hep-lat/9704011.
- [13] C. J. Morningstar and M. Peardon, Phys. Rev. **D60**, 034509 (1999), hep-lat/9901004.
- [14] C. Morningstar and M. J. Peardon, Nucl. Phys. Proc. Suppl. **83**, 887 (2000), hep-lat/9911003.
- [15] C. Liu, Chin. Phys. Lett. **18**, 187 (2001), hep-lat/0004018.
- [16] CP-PACS, T. Manke *et al.*, Phys. Rev. Lett. **82**, 4396 (1999), hep-lat/9812017.
- [17] CP-PACS, A. Ali Khan *et al.*, Nucl. Phys. Proc. Suppl. **83**, 319 (2000), hep-lat/9909133.
- [18] CP-PACS, T. Manke, Nucl. Phys. Proc. Suppl. **86**, 397 (2000), hep-lat/9909038.
- [19] I. T. Drummond, R. R. Horgan, T. Manke and H. P. Shanahan, Nucl. Phys. Proc. Suppl. **73**, 336 (1999), hep-lat/9809170.

- [20] I. T. Drummond, N. A. Goodman, R. R. Horgan, H. P. Shanahan and L. C. Stononi, *Phys. Lett.* **B478**, 151 (2000), hep-lat/9912041.
- [21] K. J. Juge, J. Kuti and C. J. Morningstar, *Nucl. Phys. Proc. Suppl.* **83**, 304 (2000), hep-lat/9909165.
- [22] C. Morningstar, *Nucl. Phys. Proc. Suppl.* **53**, 914 (1997), hep-lat/9608019.
- [23] P. Hasenfratz and F. Niedermayer, *Nucl. Phys.* **B414**, 785 (1994), hep-lat/9308004.
- [24] T. DeGrand, A. Hasenfratz, P. Hasenfratz and F. Niedermayer, *Nucl. Phys.* **B454**, 587 (1995), hep-lat/9506030.
- [25] T. DeGrand, A. Hasenfratz, P. Hasenfratz and F. Niedermayer, *Nucl. Phys.* **B454**, 615 (1995), hep-lat/9506031.
- [26] T. DeGrand, A. Hasenfratz, P. Hasenfratz and F. Niedermayer, *Phys. Lett.* **B365**, 233 (1996), hep-lat/9508024.
- [27] M. Blatter and F. Niedermayer, *Nucl. Phys.* **B482**, 286 (1996), hep-lat/9605017.
- [28] F. Niedermayer, P. Rufenacht and U. Wenger, *Nucl. Phys.* **B597**, 413 (2001), hep-lat/0007007.
- [29] W. Bietenholz and U. J. Wiese, *Nucl. Phys.* **B464**, 319 (1996), hep-lat/9510026.
- [30] W. Bietenholz, R. Brower, S. Chandrasekharan and U. J. Wiese, *Nucl. Phys.* **B495**, 285 (1997), hep-lat/9612007.
- [31] T. DeGrand, A. Hasenfratz, P. Hasenfratz, P. Kunszt and F. Niedermayer, *Nucl. Phys. Proc. Suppl.* **53**, 942 (1997), hep-lat/9608056.
- [32] P. Hasenfratz *et al.*, (2000), hep-lat/0003013.
- [33] P. Hasenfratz *et al.*, *Nucl. Phys. Proc. Suppl.* **94**, 627 (2001), hep-lat/0010061.
- [34] T. DeGrand, A. Hasenfratz and D. Zhu, *Nucl. Phys.* **B475**, 321 (1996), hep-lat/9603015.
- [35] T. DeGrand, A. Hasenfratz and D. Zhu, *Nucl. Phys.* **B478**, 349 (1996), hep-lat/9604018.
- [36] T. DeGrand, A. Hasenfratz and T. G. Kovacs, *Nucl. Phys.* **B505**, 417 (1997), hep-lat/9705009.
- [37] F. Farchioni and A. Papa, *Phys. Rev.* **D58**, 054502 (1998), hep-lat/9711030.

- [38] P. Rufenacht and U. Wenger, Nucl. Phys. Proc. Suppl. **94**, 640 (2001), hep-lat/0010057.
- [39] P. Rufenacht, *Perfect Gauge Actions on Anisotropic Lattices*, PhD thesis, University of Bern, 2001, hep-lat/0105033.
- [40] U. Wenger, *Lattice gauge theory with fixed point actions*, PhD thesis, University of Bern, 2000.
- [41] F. Niedermayer, P. Rufenacht and U. Wenger, Nucl. Phys. Proc. Suppl. **94**, 636 (2001), hep-lat/0011041.
- [42] W. Bietenholz, Int. J. Mod. Phys. **A15**, 3341 (2000), hep-lat/9911015.
- [43] M. J. Teper, Phys. Rev. **D59**, 014512 (1999), hep-lat/9804008.
- [44] M. Alford, I. T. Drummond, R. R. Horgan, H. Shanahan and M. J. Peardon, Phys. Rev. **D63**, 074501 (2001), hep-lat/0003019.
- [45] M. Luscher, Nucl. Phys. **B180**, 317 (1981).
- [46] N. Isgur and J. Paton, Phys. Rev. **D31**, 2910 (1985).
- [47] S. Perantonis, Nucl. Phys. Proc. Suppl. **9**, 249 (1989).
- [48] S. Perantonis, A. Huntley and C. Michael, Nucl. Phys. **B326**, 544 (1989).
- [49] APE, M. Albanese *et al.*, Phys. Lett. **B192**, 163 (1987).
- [50] E. Eichten, K. Gottfried, T. Kinoshita, K. D. Lane and T. M. Yan, Phys. Rev. **D21**, 203 (1980).
- [51] R. Sommer, Nucl. Phys. **B411**, 839 (1994), hep-lat/9310022.
- [52] G. S. Bali and K. Schilling, Phys. Rev. **D46**, 2636 (1992).
- [53] R. G. Edwards, U. M. Heller and T. R. Klassen, Nucl. Phys. **B517**, 377 (1998), hep-lat/9711003.
- [54] ALPHA, M. Guagnelli, R. Sommer and H. Wittig, Nucl. Phys. **B535**, 389 (1998), hep-lat/9806005.
- [55] C. J. Morningstar, K. J. Juge and J. Kuti, Nucl. Phys. Proc. Suppl. **73**, 590 (1999), hep-lat/9809098.
- [56] A. M. Ferrenberg and R. H. Swendsen, Phys. Rev. Lett. **61**, 2635 (1988).
- [57] A. M. Ferrenberg and R. H. Swendsen, Phys. Rev. Lett. **63**, 1195 (1989).
- [58] P. Minkowski and W. Ochs, Eur. Phys. J. **C9**, 283 (1999), hep-ph/9811518.
- [59] E. Klempt, (2000), hep-ex/0101031.

- [60] UKQCD, C. Michael, M. S. Foster and C. McNeile, Nucl. Phys. Proc. Suppl. **83**, 185 (2000), hep-lat/9909036.
- [61] UKQCD, C. McNeile and C. Michael, Phys. Rev. **D63**, 114503 (2001), hep-lat/0010019.
- [62] C. Bernard *et al.*, (2001), hep-lat/0104002.
- [63] B. Berg and A. Billoire, Nucl. Phys. **B221**, 109 (1983).
- [64] D.-Q. Liu, J.-M. Wu and Y. Chen, (2001), hep-lat/0103018.
- [65] D. Q. Liu and J. M. Wu, (2001), hep-lat/0105019.
- [66] M. Teper, Phys. Lett. **B183**, 345 (1987).
- [67] UKQCD, G. S. Bali *et al.*, Phys. Lett. **B309**, 378 (1993), hep-lat/9304012.
- [68] M. J. Teper, (1998), hep-th/9812187.
- [69] A. Vaccarino and D. Weingarten, Phys. Rev. **D60**, 114501 (1999), hep-lat/9910007.